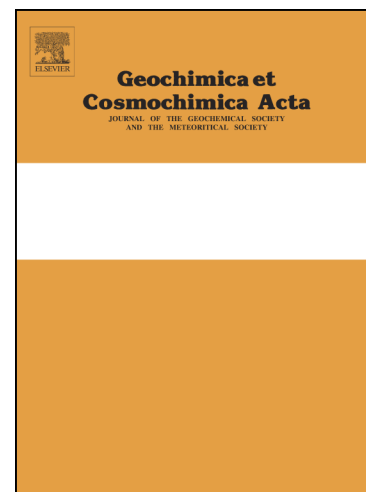# Journal Pre-proofs

The spatial footprint of hydrothermal scavenging on ^{230}Th$_{XS}$-derived mass accumulation rates

Jennifer L. Middleton, Sujoy Mukhopadhyay, Kassandra M. Costa, Frank J. Pavia, Gisela Winckler, Jerry F. McManus, Marcelle D'Almeida, Charles H. Langmuir, Peter J. Huybers

The spatial footprint of hydrothermal scavenging on ^{230}Th$_{XS}$-derived mass accumulation rates

Jennifer L. Middleton[a,*,] Sujoy Mukhopadhyay[b], Kassandra M. Costa[c], Frank J. Pavia[a,d,e], Gisela Winckler[a,d], Jerry F. McManus[a,d], Marcelle D'Almeida[b], Charles H. Langmuir[f], Peter J. Huybers[f]

[a] Lamont-Doherty Earth Observatory of Columbia University, Palisades, NY 10964, USA
[b] Department of Earth and Planetary Sciences, University of California Davis, Davis, CA 95616, USA
[c] Department of Geology and Geophysics, Woods Hole Oceanographic Institution, Woods Hole, MA 02543, USA
[d] Department of Earth and Environmental Sciences, Columbia University, New York, NY 10027, USA
[e] Now at Department of Geological and Planetary Sciences, California Institute of Technology, Pasadena, CA 91125, USA
[f] Department of Earth and Planetary Sciences, Harvard University, Cambridge, MA 02138, USA

*Corresponding author: jennym@ldeo.columbia.edu; office: 845-365-8481; fax: 845-365-8155

Abstract

Mid-ocean ridges are valuable archives of sedimentary flux records used to investigate atmospheric, oceanographic, and solid Earth responses to climate variability. Constant flux proxies, such as extraterrestrial helium-3 ($^3\text{He}_{ET}$) and excess thorium-230 ($^{230}\text{Th}_{XS}$), constrain vertical mass accumulation rates independent of the biases associated with lateral sediment transport and age model resolution. However, thorium scavenging by hydrothermal particles can perturb local $^{230}\text{Th}_{XS}$ deposition and complicate its application as a constant flux proxy in near-ridge environments. We characterize the footprint of hydrothermal scavenging on sedimentary $^{230}\text{Th}_{XS}$ using coupled $^3\text{He}_{ET}$-$^{230}\text{Th}_{XS}$ analyses in cores from the Mid-Atlantic Ridge and the Juan de Fuca Ridge. Samples deposited >10 km from the Juan de Fuca Ridge indicate reliable off-axis behavior of both constant flux proxies. In contrast, samples deposited <10 km from the Juan de Fuca Ridge axis and within the axial valley of the Mid-Atlantic ridge suggest 50-80% deficits in sedimentary $^{230}\text{Th}_{XS}$ relative to its production rate. These deficits contrast with sedimentary $^{230}\text{Th}_{XS}$ surpluses recently observed on the East Pacific Rise. The spatial footprint of hydrothermal scavenging varies globally and temporally, likely as a function of the intensity of local hydrothermal activity. The combined ridge data suggest that near-vent sediments (within ~5 km, but variable by ridge) receive relatively high $^{230}\text{Th}_{XS}$ deposition rates as a direct result of hydrothermal particle scavenging, while more distal sediments receive relatively low $^{230}\text{Th}_{XS}$ deposition rates due to diffusive loss of overlying seawater $^{230}\text{Th}_{XS}$ towards the vent. Aside from the East Pacific Rise, far-field sediments are likely to exhibit typical $^{230}\text{Th}_{XS}$ deposition rates at distances greater than ~10 km of the ridge axis. However, $^{230}\text{Th}_{XS}$ systematics within the axial valleys of slow-spreading ridges may be complicated by other factors. Combined $^3\text{He}_{ET}$-$^{230}\text{Th}_{XS}$ studies at multiple ridges are needed to further characterize the nature of hydrothermal scavenging and to evaluate the potential of sedimentary $^{230}\text{Th}_{XS}$ anomalies to record large-scale variability in past hydrothermal activity.

1. Introduction

Depositional records of climate proxies such as calcium carbonate, lithogenic material, and biogenic opal constructed from marine sediment cores provide critical constraints on atmospheric and oceanographic responses to changing climate (e.g., Adkins et al., 2006; Anderson et al., 2009; Costa et al., 2016b; Haug et al., 1999; Middleton et al., 2018; Ruddiman, 1997; Skonieczny et al., 2019; Winckler et al., 2008; Winckler et al., 2016). At more than 60,000 km in global length, mid-ocean ridges and their flanks host valuable open-ocean paleoceanographic records from above the carbonate compensation depth, where carbonate-based chronological and environmental proxies can be preserved. Near-ridge cores are additionally advantageous because they can be used to investigate millennial- and orbital-scale variations in submarine hydrothermal activity (Auffret et al., 1996; Cave et al., 2002; Cherkashev, 1995; Costa et al., 2017; Frank et al., 1994; German et al., 1997; Lund et al., 2016; Middleton et al., 2016). Such records are an essential tool for evaluation of the hypothesis that submarine volcanic centers are sensitive to glacially-driven changes in sea level and to understand how variations in the solid Earth influence ocean chemistry (Costa et al., 2017; Crowley et al., 2015; Huybers and Langmuir, 2009; Lund et al., 2016; Lund and Asimow, 2011; Lund et al., 2019; Middleton et al., 2016; Tolstoy, 2015).

Traditionally, the fluxes of hydrothermal, authigenic, biogenic, and lithogenic sediments have been derived from stratigraphic mass accumulation rates based on the sediment mass between a core's age model tie-points. These stratigraphic accumulation rates can be biased by lateral sediment transport and are limited by age model resolution (Higgins et al., 2002; Marcantonio et al., 2001b; Marcantonio et al., 1996; Suman and Bacon, 1989). Sediments deposited atop the rough bathymetry of a mid-ocean ridge may be especially subject to variations in sediment focusing and winnowing that can convolute interpretation of stratigraphically-derived accumulation rate records from these settings (Costa and McManus, 2017; Middleton et al., 2018). In contrast, constant flux proxies, such as extraterrestrial helium-3 ($^3He_{ET}$; Farley, 1995; Farley and Patterson, 1995; Marcantonio et al., 1995; Takayanagi and Ozima, 1987; Winckler et al., 2005) and excess thorium-230 ($^{230}Th_{XS}$; Bacon, 1984; Francois et al., 2004; McManus et al., 1998; Suman and Bacon, 1989), can be used to calculate vertical mass accumulation rates that are independent of age model limitations and sediment focusing effects. Consequently, constant flux proxies provide a means to constrain depositional variability in sedimentary inputs at any resolution, even in complex depositional environments (e.g., Costa and McManus, 2017; Higgins et al., 2002; Middleton et al., 2018).

The utility of $^3He_{ET}$ and $^{230}Th_{XS}$ as constant flux proxies derives from the presumed constant deposition rate of these nuclides to the seafloor. ^3He is primarily delivered to marine sediments via interplanetary dust particles (IDPs; Farley, 1995; Nier and Schlutter, 1993; Takayanagi and Ozima, 1987). IDPs are dominantly sourced from the asteroid belt and active comets and thus contain implanted solar helium with a $^3He/^4He$ ratio of 2.4×10^{-4} (or 170 R_A, where R_A denotes the atmospheric $^3He/^4He$ value; Nier and Schlutter, 1992). The $^3He/^4He$ ratio of this extraterrestrial helium is several orders of magnitude higher than the $\sim 2 \times 10^{-8}$ (0.01 R_A) value of typical terrigenous materials (Farley and Patterson, 1995; Marcantonio et al., 1998). The $^3He_{ET}$ concentration of marine sediments is determined by subtracting the terrigenous component from the total ^3He using a two-endmember mixing model. Compiled marine and ice core records suggest a consistent, globally uniform, Quaternary $^3He_{ET}$ influx with a mean and standard deviation of $8.0 \pm 1.2 \times 10^{-13}$ cc STP cm^{-2} kyr^{-1} (McGee and Mukhopadhyay, 2013). The retention of $^3He_{ET}$ in limestones dating to ~ 480 Ma suggests that post depositional diffusive loss of $^3He_{ET}$ is minimal (Patterson et al., 1998), especially over the timescales investigated in this study.

Unlike $^3He_{ET}$, ^{230}Th is generated through the decay of seawater ^{234}U and is rapidly scavenged by particles that sink to the sediments below (Bacon and Anderson, 1982). Seawater uranium is well mixed and produces ^{230}Th at a uniform rate throughout the water column (Andersen et al., 2010). Thus, the sedimentary deposition rate of ^{230}Th at a given location is a function of the known activity of ^{234}U in seawater and the height of the overlying water column (Bacon, 1984). Sedimentary $^{230}Th_{XS}$ concentrations are determined by correcting total ^{230}Th for lithogenic ^{230}Th and for authigenic ingrowth from in situ ^{234}U decay (e.g., Francois et al., 2004; Henderson et al., 2003). Resulting values are adjusted for $^{230}Th_{XS}$ decay using the sediment sample age to yield the initial concentration (for simplicity, all subsequent references to $^{230}Th_{XS}$ indicate initial $^{230}Th_{XS}$). Given the 75.6 kyr half-life of ^{230}Th, uncertainties in the determination of $^{230}Th_{XS}$ increase with age and applications of $^{230}Th_{XS}$ as a constant flux proxy are limited to the past ~ 500 ka (e.g., Costa and McManus, 2017; Marcantonio et al., 1996; Winckler et al., 2008).

Thorium scavenging by metalliferous hydrothermal precipitates can complicate near-ridge applications of $^{230}Th_{XS}$ as a constant flux proxy. GEOTRACES water column profiles from the Mid-Atlantic Ridge, the East Pacific Rise, and the Gakkel Ridge reveal strong deficits in seawater ^{230}Th concentrations coincident with hydrothermal plume position, even several km off-axis (Hayes et al., 2015; Pavia et al., 2018; Valk et al., 2018). These seawater ^{230}Th deficits result from scavenging of seawater Th onto hydrothermal Mn and Fe-oxyhydroxide particles that ultimately fall out of the water column to the sediments below. Sediment recovered in close proximity to hydrothermal systems (<20 km) can exhibit anomalously high $^{230}Th_{XS}$ concentrations (Frank et al., 1994; German and Sparks, 1993; German et al., 1997; Shimmield and Price, 1988). On the East Pacific Rise, near-vent (<200 m) sediment traps and near-axis (~8 km) sediment cores reveal $^{230}Th_{XS}$ deposition rates that are 3 to 4-fold higher than the overlying water column production rate (German et al., 2002; Lund et al., 2019). In such environments, direct interpretation of the $^{230}Th_{XS}$-derived sediment accumulation rate would produce an underestimate. For example, the relatively high rates of $^{230}Th_{XS}$ deposition at the East Pacific Rise would yield $^{230}Th_{XS}$-derived mass accumulation rates that are 3 to 4-times lower than the true vertical sediment flux (German et al., 2002; Lund et al., 2019).

Consequently, informed interpretation of near-ridge $^{230}Th_{XS}$-derived mass accumulation rate records necessitates spatial and temporal characterization of hydrothermal influences on $^{230}Th_{XS}$ systematics. Anomalous $^{230}Th_{XS}$ burial can be quantified using $^{3}He_{ET}$-derived $^{230}Th_{XS}$ deposition rate records (e.g., Lund et al., 2019) because $^{3}He_{ET}$ is insensitive to hydrothermal processes (see Section 4.3.1 for elaboration). A refined understanding of hydrothermal scavenging yields broader insights into the nature of hydrothermal activity and its effects on marine distributions of iron and other important trace metals. Further, examination of anomalous $^{230}Th_{XS}$ deposition rates may provide a valuable new proxy for the occurrence of past episodes of hydrothermal activity.

We evaluate here the performance of the $^{230}Th_{XS}$ constant flux proxy near mid-ocean ridges using coupled-helium, thorium, and trace metal analyses in sediment cores from the Mid-Atlantic Ridge and the Juan de Fuca Ridge. We combine new thorium isotope data with existing Mid-Atlantic Ridge records (Middleton et al., 2016; 2018) and new Broken Spur hydrothermal element data. We also present new helium isotope data spanning the past 600 ka that complement existing SeaVOICE thorium and hydrothermal datasets from the Cleft Segment of the Juan de Fuca Ridge (Costa and McManus, 2017; Costa et al., 2017). This unprecedented suite of data includes $^{3}He_{ET}$-derived $^{230}Th_{XS}$ deposition rates for over 200 near-ridge samples.

2. Sampling and Methods

2.1 Study Regions

The Mid-Atlantic Ridge and Juan de Fuca Ridge sediment cores examined in this study were chosen to evaluate $^{3}He_{ET}$-$^{230}Th_{XS}$ systematics across variations in ridge-proximity, intensity of local hydrothermal deposition, and ridge bathymetry (Figure 1). On the intermediate spreading-rate Juan de Fuca Ridge, active centers of high-temperature hydrothermal activity typically occur along the spreading axis of the ridge (Beaulieu et al., 2013). Over the past 600 kyr, plate motions have transported the Juan de Fuca Ridge cores about 18 km off-axis at a rate of 30 mm/yr

4

(Govers and Meijer, 2001). On the slow-spreading Mid-Atlantic Ridge, the spreading axis and active centers of high-temperature hydrothermal circulation sit within an axial valley averaging ~10 km across (Beaulieu et al., 2013; Murton et al., 1994). Sediments deposited within the axial valley move away from the spreading axis at rates of 11-13 mm/yr, but intense hydrothermal activity can occur "off-axis" within the valley on crust as old as 100 ka (Humphris and Tivey, 2000; McGregor and Rona, 1975). Over the 70 kyr interval examined, the Mid-Atlantic Ridge cores have migrated less than 1 km away from their local centers of hydrothermal activity.

2.1.1. Mid-Atlantic Ridge

Gravity core KN207-2-GGC3 (26.14°N, 44.80°W, 3433 m water depth, 82 cm core length) spans the past 50 ka and was recovered within 1 km of the relict Mir hydrothermal zone and 3 km of the active TAG mound in the axial valley of the TAG Segment of the Mid-Atlantic Ridge (Figure 1) during cruise KN207-2 of the *R/V Knorr*. Helium isotope analyses and hydrothermal and terrigenous contributions to GGC3 are reported in Middleton et al. (2016). This work uses the revised GGC3 chronology of Middleton et al. (2018) and presents new Th isotope data for 27 samples.

Nearly 400 km to the northeast of TAG, gravity core KN207-2-GGC6 (29.21°N, 43.23°W, 3018 m water depth, 147 cm core length) was also recovered during cruise KN207-2 (Figure 1). GGC6 sediments span the past 70 ka and were retrieved from the axial valley of the Broken Spur Segment of the Mid-Atlantic Ridge, within 7 km of the active Broken Spur hydrothermal system. Sediment chronology, core description, helium isotope analyses, and terrigenous contributions for GGC6 are reported in Middleton et al. (2018). This study presents new hydrothermal Fe and Cu concentration data throughout GGC6, as well as new Th isotope data for 45 GGC6 samples.

2.1.2 Juan de Fuca Ridge

Piston cores AT26-19-09PC (44.89°N, 130.64°W, 2678 m water depth, 766 cm core length) and AT26-19-12PC (44.90°N, 130.50°W, 2689 m water depth, 550 cm core length) were recovered as part of a suite of cores retrieved from the Cleft Segment of the Juan de Fuca Ridge in the Northeast Pacific during the SeaVOICE cruise (AT26-19) of the *R/V Atlantis* (Figure 1; Costa et al., 2016). Cores 09PC (spanning the past 440 ka) and 12PC (spanning the past 600 ka) were retrieved 30 and 18 km, respectively, from the spreading center of the Cleft Segment and its known active hydrothermal fields. The bottom of 12PC is terminated by the presence of basalt rock and fragments of basalt glass are observed in 12PC sediments deposited prior to 545 ka (Ferguson et al., 2017). The 09PC record does not contain basalt.

Sediment chronologies, thorium isotope analyses, and hydrothermal element data for the Juan de Fuca Ridge cores are reported in Costa et al. (2016), Costa and McManus (2017), and Costa et al. (2017), respectively. Reported $^{230}Th_{XS}$ data for 12PC is limited to the past 420 ka due to increasing analytical uncertainties in the oldest sediments (Costa and McManus, 2017). This work presents new helium isotope data for both 12PC and 09PC. Extensive helium isotope analyses were performed in 12PC due to its closer proximity to the ridge axis (18 km). Sparse helium analyses were performed in 09PC to evaluate the spatial reproducibility of $^3He_{ET}$-derived vertical sediment rain rates in the SeaVOICE sediments.

2.2. Helium Isotope Analyses

Helium isotope analyses for the Juan de Fuca Ridge cores (09PC and 12PC; Supplemental Table S1) were determined using 0.5 g initial aliquots of dry bulk sediment at the UC Davis Noble Gas Laboratory following the methods of Middleton et al. (2016) with slight modification as discussed below. Helium sampling intervals coincide with those used for thorium isotope analyses in Costa and McManus (2017).

Mantle-derived helium in mid-ocean ridge basalt is a potential contaminant to the application of $^3He_{ET}$ in near-ridge sediments (Graham, 2002). Juan de Fuca Ridge samples were typically sieved during preparation, with helium analyses performed solely in the <64 um fraction, in order to reduce possible contamination from coarse basalt fragments. A subset of samples from 12PC, indicated by 'star' in Supplemental Table S1, were lightly crushed with a mortar and pestle and subsequently processed without sieving. Samples for which both sieved and unsieved helium analyses were performed do not exhibit systematic offsets in $^3He_{ET}$ concentrations (Supplemental Figure S1).

Sample $^3He_{ET}$ concentrations were calculated assuming a two component mixture of IDP helium with a $^3He/^4He$ ratio of 170 R_A (Nier and Schlutter, 1992) and terrigenous helium with a $^3He/^4He$ ratio of 0.01 R_A (Farley and Patterson, 1995). Using these end-member values, $^3He_{ET}$ represents ~99% of total ^3He measured for the average Juan de Fuca Ridge sample. The conclusions of this work are not sensitive to uncertainties in the helium isotope values of IDP and terrigenous end-members. If an extreme terrigenous $^3He/^4He$ ratio of 0.10 R_A (Marcantonio et al., 1998) is instead assumed, average $^3He_{ET}$ -derived vertical rain rates would be ~10% higher than the values reported in this study.

Uncertainties in sediment $^3He_{ET}$ concentrations are dominated by the heterogeneous distribution of rare large and helium-rich IDPs that are not representatively sampled in typical sediment aliquots (Farley et al., 1997; Marcantonio et al., 1999; Mukhopadhyay et al., 2001). The magnitude of this 'nugget effect' is a function of the area-time product of the samples measured, calculated by dividing the sample aliquot mass (in g) by the stratigraphic mass accumulation rate (in g m^{-2} a^{-1}). A typical area-time product of 0.25 m^{2}a yields a 1σ uncertainty in sedimentary $^3He_{ET}$ concentrations of ~20% (Farley et al., 1997; Mukhopadhyay et al., 2001), much larger than the instrumental uncertainty of ~4% for helium isotope measurements. The 0.5 g sample aliquots and average stratigraphic mass accumulation rates of the Juan de Fuca Ridge (09PC and 12PC) sediments result in a lower area-time product of ~0.10 m^{2}a that drives a higher uncertainty.

In lieu of the nugget effect, the 1σ uncertainty in $^3He_{ET}$ concentrations for a single aliquot analysis of Juan de Fuca Ridge sediment was determined from the reproducibility of a suite of 164 replicated sample pairs. The observed distribution of fractional differences in $^3He_{ET}$ concentrations between the replicated samples is reasonably approximated as a Gaussian with 1σ of 39% (Supplemental Figure S2). This 39% 1σ uncertainty is reduced in replicated samples by a scaling of $0.39/\sqrt{n}$, where n is the number of aliquots analyzed.

2.2.2. $^3He_{ET}$-derived Accumulation Rates

Bulk sediment accumulation rates derived from $^3He_{ET}$ ($^{3He}\Phi_{sed}$) were computed by dividing the known $^3He_{ET}$ influx from space (f_{3He}) by the average $^3He_{ET}$ concentration of each sample [$^3He_{ET}$] using the following equation:

$$^{3He}\Phi_{sed} = \frac{f_{3He}R}{[^3He^{ET}]}$$ EQ. 1

where f_{3He} is $8.0 \pm 1.2 \times 10^{-13}$ cm^3 STP cm^{-2} kyr^{-1} (McGee and Mukhopadhyay, 2013) and R is the fractional retentivity of He within the sediments (Farley, 1995). Given the high level of $^3He_{ET}$ retention observed in early Phanerozoic limestones (Patterson et al., 1998), a constant R value of 1 is assumed for the Pleistocene sediments examined here.

The $^3He_{ET}$-derived sediment focusing factor (Ψ_{He}), a quantitative measure of lateral sediment transport, is then computed from the following equation:

$$\Psi^{He} = \frac{\int_{z_1}^{z_2}[^3He^{ET}]\rho_b dz}{f(t_2 - t_1)}$$ EQ 2.

where z is depth in the core, ρ_b is the sediment dry bulk density, f is the known $^3He_{ET}$ influx from space as above, and t_1 and t_2 are the sediment ages at depths z_1 and z_2.

2.3. Thorium Isotope Analyses and $^{230}Th_{XS}$-derived Accumulation Rates

Mid-Atlantic Ridge (GGC3 and GGC6) thorium isotope measurements and $^{230}Th_{XS}$-derived mass accumulation rates (Supplemental Table S2) were determined following the methods of Costa and McManus (2017) using the same sampling depths as used for helium analyses (Middleton et al., 2016; 2018). Briefly, 100 mg sample aliquots were spiked with ^{229}Th and ^{236}U, digested in concentrated acids, chromatographically separated, and measured via inductively-coupled plasma mass spectrometry at Lamont-Doherty Earth Observatory following the methods described by (Fleisher and Anderson, 2003).

Complete procedural replicates (n = 4) of the VOICE Internal MegaStandard (VIMS), comprised of homogenized sediments from the Juan de Fuca Ridge, were within 3% of previously published values (Costa and McManus, 2017) and had 1σ reproducibility of ^{230}Th (0.23%), ^{232}Th (2.0%), and ^{238}U (4.2%). Lithogenic and authigenic ^{230}Th contributions were subtracted assuming an Atlantic basin $^{238}U/^{232}Th$ activity ratio of 0.6 (Henderson et al., 2003). The relatively young ages of the Mid-Atlantic Ridge samples (less than one half-life of ^{230}Th), as well as the low lithogenic (<8% of total ^{230}Th) and authigenic (<2% of total ^{230}Th) corrections result in 1σ uncertainties of ~2% or less in the determination of $^{230}Th_{XS}$.

Bulk sediment mass accumulation rates derived from $^{230}Th_{XS}$ ($^{230Th}\Phi_{sed}$) were computed using the following equation:

$$^{230Th}\Phi_{sed} = \frac{\beta * z}{[230ThXS]}$$ EQ. 3

Where β is the seawater ^{230}Th production rate of 2.555 x 10^{-5} dpm/cm^3 kyr, z is the height of the water column above each core location, and [^{230}Th$_{XS}$] is the ^{230}Th$_{XS}$ concentration of each sample at the time of deposition in dpm/g.

The precise z value of mid-ocean ridge surface sediments increases with time on the seafloor due to the off-axis motion of the underlying crust. On the Juan de Fuca Ridge, for example, the 12PC ^{230}Th$_{XS}$ record begins at ~425 ka, when 12PC was likely positioned 5 km off-axis at an approximate depth of 2400 m (Figure 1). This ~10% change in depth, relative to the current value of 2689 m, is associated with a ~10% decrease in the ^{230}Th$_{XS}$ production rate of the overlying water column for these oldest samples (EQ. 3). The effect is smaller for GGC3 and GGC6 on the Mid-Atlantic Ridge due to slow-spreading ridge morphology and the brevity of these records. Given the uncertainties associated with the exact time-depth trajectory of each sediment core, the ^{230}Th$_{XS}$ data presented in this work is exclusively determined using modern z values. This assumption does not significantly alter the conclusions of this work.

2.4. Hydrothermal Contributions

Hydrothermal contributions to GGC6 (Broken Spur, Mid-Atlantic Ridge; Supplemental Table S3) were determined from analyses of Fe, Cu, and Ti concentrations performed via ICP-MS analyses at Harvard University as described in Middleton et al. (2016; 2018).

The hydrothermal components (X$_{HT}$) of total Fe and Cu were distinguished from lithogenic contributions following the relationship:

$$X_{HT} = X_{total} - (X/Ti)_{lith} * Ti_{total} \qquad \text{EQ. 4}$$

where (X/Ti)$_{lith}$ represents the lithogenic ratio of the average upper continental crust (~11.7 wt.%/wt.% and 83 ppm/wt.% for Fe, and Cu, respectively (Taylor and McLennan, 1995).

Component-specific fluxes (Φ_x) were then calculated as follows:

$$\Phi_x = [X]_{sed} * \Phi_{sed} \qquad \text{EQ. 5}$$

where [X]$_{sed}$ is the sediment concentration of the component of interest, and Φ_{sed} may be either the ^{3}He$_{ET}$- or ^{230}Th$_{XS}$-derived mass accumulation rate.

3. Results

3.1 Mid-Atlantic Ridge

3.1.1. Broken Spur Hydrothermal Record

Despite the proximity of GGC6 to the Broken Spur vent field, the Fe and Cu data indicate only weak hydrothermal deposition over the past 70 ka (Figure 2). Fe$_{HT}$ typically accounts for 5% of the total Fe in GGC6 sediments. However, many samples are associated with negative Fe$_{HT}$

concentrations, suggesting that uncertainties in the lithogenic input composition may be larger than GGC6 concentrations of hydrothermal materials. Rather than reflect the average upper continental crust (with Fe/Ti ~11.7 wt.%/wt.%; Taylor and McLennan, 1995), lithogenic contributions to the GGC6 sediments may contain a combination of small basalt fragments (Fe/Ti ~8.3 wt.%/wt.%; Gale et al., 2013) and Northwest African dust (Fe/Ti ranging from ~6 to 11 wt.%/wt.%; Castillo et al., 2008). Utilization of a lithogenic Fe/Ti ratio of 7.4 wt.%/wt.% in Eq. 4 yields a GGC6 Fe_{HT} record without negative values. Assuming this lithogenic input, Fe_{HT} accounts ~37% of total sedimentary Fe and Fe_{HT} fluxes in GGC6 vary from 0 to 3 mg/cm^{2}kyr.

Estimates of GGC6 Cu_{HT} concentrations are also sensitive to lithogenic input composition. Using the 83 ppm/wt.% Cu/Ti ratio of average upper continental crust (Taylor and McLennan, 1995), Cu_{HT} accounts for ~80% of total Cu in typical GGC6 sediments. While the ~80 ppm/wt% Cu/Ti ratio of mid-ocean ridge basalts is similar to that of average upper continental crust (Gale et al., 2013), Cu/Ti values in Northwest African dust range from ~200 to >2000 ppm/wt.% (Castillo et al., 2008). If a conservatively low Northwest African dust Cu/Ti value of ~375 ppm/wt% is instead used in EQ. 4, hydrothermal Cu would account for ~20% of total Cu in average GGC6 sediments.

Using a lithogenic endmember composition equivalent to the average upper continental crust, $^3He_{ET}$-derived Fe_{HT} and Cu_{HT} fluxes remain <1 mg/cm^2 kyr and <25 µg/cm^2 kyr, respectively, in the Broken Spur record over the past 70 ka. These values are generally lower than even the lowest Fe_{HT} and Cu_{HT} fluxes observed in the TAG sediments (GGC3). The temporal patterns of Fe_{HT} and Cu_{HT} flux observed in GGC6 are also distinct from those observed in GGC3 (Figure 2). Consequently, our new data indicate that the two Mid-Atlantic Ridge cores have received significantly different levels of direct hydrothermal precipitation.

3.1.2. Mid-Atlantic Ridge Helium-Thorium Comparison

The magnitudes of $^{230}Th_{XS}$-derived mass accumulation rates are persistently higher than $^3He_{ET}$-derived mass accumulation rates over the last glacial period throughout each core on the Mid-Atlantic Ridge (GGC3 and GGC6; Figure 3a-b; Supplemental Table S4). The $^3He_{ET}$-derived accumulation rates vary between 0.2 - 0.5 g/cm^2 kyr at TAG (GGC3) and between 0.2 – 1.3 g/cm^2 kyr at Broken Spur (GGC6). In contrast, the $^{230}Th_{XS}$-derived accumulation rates over this interval vary between 0.6 – 1.0 g/cm^2 kyr and 0.7 – 2.4 g/cm^2 kyr for the TAG and Broken Spur records, respectively.

The $^{230}Th_{XS}$-derived accumulation rates also exhibit a distinct pattern of temporal variability relative to those derived from $^3He_{ET}$ in both Mid-Atlantic Ridge sediment cores (Figure 3a-b). In the TAG record, for example, the highest $^3He_{ET}$-derived accumulation rates occur during the deglacial period and early Holocene (~18 – 8 ka), while the highest $^{230}Th_{XS}$-derived accumulation rates occur during Marine Isotope Stage 3 (MIS 3, ~57 – 39 ka; Figure 3a). These distinct temporal patterns manifest as a weak correlation between $^{230}Th_{XS}$- and $^3He_{ET}$- derived mass accumulation rates at Broken Spur (GGC6; $R^2 = 0.41$, $p < 0.01$; Supplemental Figure S3a) and as no significant correlation between $^{230}Th_{XS}$- and $^3He_{ET}$- derived mass accumulation rates at TAG (GGC3; $R^2 = 0.12$, $p = 0.12$; Supplemental Figure S3a). We note that the P-values presented for each correlation in this study represent 1-sided P-values estimated using a null

9

distribution of R-values generated from 10,000 comparisons of phase randomized surrogate data in order to reduce the influence of autocorrelation within each sedimentary record (e.g., Theiler et al., 1992).

The sedimentary $^{230}Th_{XS}/^{3}He_{ET}$ ratio can be used to compare $^{3}He_{ET}$ and $^{230}Th_{XS}$ systematics across multiple study regions. Measured $^{230}Th_{XS}/^{3}He_{ET}$ values are divided by the local $^{230}Th_{XS}/^{3}He_{ET}$ production ratio (R_P, defined as $(\beta * z)/f_{3He}$) to eliminate depth-dependent variability in $^{230}Th_{XS}$ deposition rates between core locations. The normalized $^{230}Th_{XS}/^{3}He_{ET}$ ratio is equivalent to the $^{3}He_{ET}$-derived $^{230}Th_{XS}$ deposition rate, relative to the local $^{230}Th_{XS}$ production rate. When $^{230}Th_{XS}/^{3}He_{ET}$ = 1 R_P, the $^{3}He_{ET}$- and $^{230}Th_{XS}$-derived mass accumulation rates are equal and the local $^{230}Th_{XS}$ deposition rate equals the water column production rate. When $^{230}Th_{XS}/^{3}He_{ET}$ < 1 R_P, the $^{230}Th_{XS}$-derived mass accumulation rate is *higher* than the $^{3}He_{ET}$-derived mass accumulation rate and the local $^{230}Th_{XS}$ deposition rate is *lower* than the water column production rate (indicating a deficit of $^{230}Th_{XS}$). The inverse applies when $^{230}Th_{XS}/^{3}He_{ET}$ > 1 R_P (indicating a surplus of $^{230}Th_{XS}$).

Mid-Atlantic Ridge $^{230}Th_{XS}/^{3}He_{ET}$ values vary from 0.2 to 0.9 R_P over the past 70 ka and, intriguingly, exhibit similar patterns of variability at both the TAG and Broken Spur study areas (Figure 4a). The $^{230}Th_{XS}/^{3}He_{ET}$ records of both GGC3 and GGC6 reach a minimum of 0.2 R_P, five times lower than the production ratio, at ~25 ka, and typically overlap over the past 35 kyr. This apparent synchronization between two axial valley cores located >350 km apart suggests that the observed variations in Mid-Atlantic Ridge $^{230}Th_{XS}/^{3}He_{ET}$ ratios may be partially influenced by a single, regional-scale mechanism.

3.2 Juan de Fuca Ridge

3.2.1. Juan de Fuca Ridge Helium-Thorium Comparison

In contrast to the Mid-Atlantic Ridge, $^{230}Th_{XS}$ and $^{3}He_{ET}$-derived mass accumulation rates in most samples from the Juan de Fuca Ridge do not exhibit a systematic offset (09PC and 12PC; Figure 3c-d; Supplemental Table S5). In 09PC, $^{230}Th_{XS}$- and $^{3}He_{ET}$- derived sediment accumulation rates are correlated with an R^2 of 0.38 (p < 0.01) and tend to overlap in magnitude within 1 sigma error throughout the full 440 ka record (Figure 3c). When the full 12PC record is examined, $^{230}Th_{XS}$- and $^{3}He_{ET}$-derived sediment accumulation rates are not correlated (R^2 = 0.12, p = 0.02; Supplemental Figure S3). However, the correlation is improved when 12PC is divided into sediments that are younger than 300 ka (R^2 = 0.49, p < 0.01) and those that are older than 300 ka (R^2 = 0.47, p < 0.01). Notably, 12PC samples younger than 300 ka yield $^{230}Th_{XS}$-derived accumulation rates that overlap within error of those derived from $^{3}He_{ET}$, while $^{230}Th_{XS}$-derived accumulation rates in older samples are systematically higher (Figure 3d).

With the exception of the oldest 09PC sediments and 12PC sediments older than 300 ka, $^{230}Th_{XS}/^{3}He_{ET}$ ratios in the Juan de Fuca Ridge cores do not deviate systematically from the production ratio of 1 R_P (Figure 4b). 09PC exhibits $^{230}Th_{XS}/^{3}He_{ET}$ ratios varying from 0.2 to 2.3 R_P, with a mean and standard deviation of 1.1 ± 0.5 R_P. Compared with the full record, 09PC samples older than 410 ka generally exhibit higher $^{230}Th_{XS}/^{3}He_{ET}$ ratios, with a mean and standard deviation of 1.6 ± 0.6 R_P. The shift to higher $^{230}Th_{XS}/^{3}He_{ET}$ values in the oldest 09PC

sediments may result from the increasing effects of uncertainty associated with lithogenic and authigenic ^{230}Th corrections in the determination of ^{230}Th$_{XS}$ concentrations near the ^{230}Th age limit. In 12PC, sediments younger than 300 ka are similar to 09PC, with ^{230}Th$_{XS}$/^{3}He$_{ET}$ ratios varying from 0.3 to 1.6 R$_P$. The mean ^{230}Th$_{XS}$/^{3}He$_{ET}$ value in 12PC sediments <300 ka is slightly lower than 09PC, at 0.8 ± 0.3 R$_P$. Overlap between the average observed ^{230}Th$_{XS}$/^{3}He$_{ET}$ ratios and the production ratio suggest that, over orbital timescales, both constant flux proxies are performing as expected in these youngest Juan de Fuca Ridge sediments, deposited furthest from the ridge axis.

The 12PC sediments deposited prior to 300 ka, however, exhibit ^{230}Th$_{XS}$/^{3}He$_{ET}$ ratios distinct from contemporaneous sediments in 09PC and significantly lower than the production ratio (Figure 4b). The 12PC ^{230}Th$_{XS}$/^{3}He$_{ET}$ values broadly decrease from 0.6 R$_P$ at 300 ka to 0.06 R$_P$ at 400 ka, with a mean of 0.34 ± 0.14 R$_P$. Given its current position ~18 km from the Cleft Segment spreading axis and assuming a constant half-spreading rate of 30 mm/yr (Govers and Meijer, 2001), 12PC sediments older than 300 ka were deposited within 9 km of the ridge axis. In comparison, the oldest sediments in 09PC were deposited at least 17 km off-axis. Thus, the lowest ^{230}Th$_{XS}$/^{3}He$_{ET}$ values in the Juan de Fuca Ridge data occur in sediments deposited in closest proximity to the nearby ridge (Figure 5). As off-axis distance increases, observed ^{230}Th$_{XS}$/^{3}He$_{ET}$ ratios in the Juan de Fuca Ridge sediments approach the value predicted under the assumptions of constant flux.

3.2.2. Extended Flux Record at the Juan de Fuca Ridge

The ^{3}He$_{ET}$ data presented in this work extend the 12PC mass accumulation rate record beyond the available ^{230}Th$_{XS}$ data from ~420 ka to ~600 ka (Figure 3d). The extended record reveals higher mass accumulation rates in sediments older than ~500 ka than are observed in either the ^{3}He$_{ET}$- or ^{230}Th$_{XS}$- based records of younger 12PC sediments. The maximum 12PC ^{3}He$_{ET}$-derived sediment accumulation rates occur between 500 and 550 ka. This period coincides with Marine Isotope Stages 13 and 14 (MIS 13 and MIS 14) and suggests a distinct depositional environment in the history of 12PC.

4. Discussion

4.1. Weak Hydrothermal Deposition at Broken Spur

The weak record of hydrothermal accumulation in GGC6 may result from bathymetric shielding of the core location from the nearby hydrothermal plume (Figure 1). A bathymetric high reaching ~300 m above the active Broken Spur vent field prevents the modern extent of the hydrothermal plume from reaching the GGC6 core site and depositing hydrothermal precipitates (e.g., German et al., 1999). The lack of a strong hydrothermal signal within the GGC6 sedimentary record suggests that the Broken Spur hydrothermal plume has not risen significantly in excess of 300 m above its originating vent field within the past 70 ka. Alternatively, prevailing currents within the axial valley may have consistently inhibited transport of the Broken Spur plume northwards to the GGC6 core location over the past 70 ka. These hypotheses could be tested using an organized suite of sediment cores recovered at varying elevations around the Broken Spur vent field.

4.2. Reliable Off-axis Behavior of $^3He_{ET}$ and $^{230}Th_{XS}$

Sediments deposited >10 km from the local ridge axis (i.e., 09PC and the youngest samples from 12PC on the Juan de Fuca Ridge) exhibit $^3He_{ET}$ and $^{230}Th_{XS}$ behavior that is consistent with the expected deposition rates for these isotope systems. Though it has been speculated in prior work that the $^3He_{ET}$ input flux to the seafloor may vary latitudinally (e.g., Hayes et al., 2017), the off-axis Juan de Fuca Ridge $^{230}Th_{XS}/^3He_{ET}$ ratios do not exhibit any significant deviation from the global Quaternary average (Figure 6). Rather, the general agreement between $^3He_{ET}$- and $^{230}Th_{XS}$-derived sediment accumulation rates in these samples is similar to observations from non-hydrothermal environments in the Atlantic, Equatorial Pacific, and Equatorial Indian ocean basins (Figure 6; Marcantonio et al., 2001a; Marcantonio et al., 2001b; Marcantonio et al., 1996; Marcantonio et al., 1995; Marcantonio et al., 1999; McGee et al., 2010). Combined, the global suite of off-axis paired $^3He_{ET}$-$^{230}Th_{XS}$ records highlight the reliability of these completely independent proxies in typical pelagic environments over a wide range of latitudes.

Similarity in the $^3He_{ET}$- and $^{230}Th_{XS}$- derived accumulation rates in the farthest off-axis Juan de Fuca Ridge sediments additionally demonstrates the utility of these systems to constrain vertical sediment fluxes despite the presence of considerable lateral sediment transport. The $^{230}Th_{XS}$-derived focusing factors in 09PC and in the <300 ka samples of 12PC (Costa and McManus, 2017) vary from less than 0.25 (indicating strong winnowing) to at least 3 (indicating focusing). Our results suggest that the carrier particles of $^3He_{ET}$ and $^{230}Th_{XS}$ are not fractionated from each other by lateral transport processes within this range of focusing intensity. This result is consistent with prior observations from the Blake Ridge, where $^3He_{ET}$ and $^{230}Th_{XS}$ exhibit general agreement, despite sediment focusing factors >10 (McGee et al., 2010).

Further, the Juan de Fuca Ridge data indicate reliable utilization of $^{230}Th_{XS}$ as a constant flux proxy at distances much closer to the nearby ridge axis (~10 km) than have been observed along the fast-spreading South East Pacific Rise, where anomalous $^3He_{ET}$-derived $^{230}Th_{XS}$ deposition rates were found as far as 28 km off-axis (Figure 7a; Lund et al., 2019). Such spatial variability is likely to arise in the manifestation of hydrothermal scavenging on $^{230}Th_{XS}$ deposition rates due to regional differences in the magnitude and transport of local hydrothermal emissions associated with variations in ridge spreading rate (e.g., Baker and German, 2004).

4.3. Near-axis Performance of $^3He_{ET}$ and $^{230}Th_{XS}$

In contrast to the >10 km off-axis samples, large discrepancies between $^3He_{ET}$ and $^{230}Th_{XS}$-derived accumulation rates, indicated by $^{230}Th_{XS}/^3He_{ET}$ ratios outside of the 0.5 to 2 R_P range, occur in sediments deposited closer to the ridge axis (12PC sediments >300 ka on the Juan de Fuca Ridge; Figure 5) and within the axial valley itself (both GGC3 and GGC6 on the Mid-Atlantic Ridge; Figure 4a). This observation is consistent with the hypothesis that mid-ocean ridge hydrothermal activity drives anomalous rates of $^{230}Th_{XS}$ deposition and interferes with the utilization of $^{230}Th_{XS}$ as a constant flux proxy in near-axis environments. However, what constitutes a 'near-axis' setting appears to vary from ridge to ridge. The spatial scale for large anomalies observed on the East Pacific Rise (e.g., Lund et al., 2019), for example, is not directly transferable to other ridge settings.

12

The near-axis Juan de Fuca Ridge and Mid-Atlantic Ridge samples generally exhibit $^{230}Th_{XS}/^{3}He_{ET}$ values that are lower than the predicted production ratio and suggestive of either excess $^{3}He_{ET}$ or depleted $^{230}Th_{XS}$. These Juan de Fuca Ridge and Mid-Atlantic Ridge observations are in direct contrast to observations from the East Pacific Rise, where observations indicate a surplus of $^{230}Th_{XS}$ (Lund et al., 2019; German et al., 2002). We first examine the possibility of excess $^{3}He_{ET}$ deposition in our near-axis samples before elaborating upon hydrothermal drivers of $^{230}Th_{XS}$ depletion.

4.3.1. Potential Sources of Excess $^{3}He_{ET}$

Near-axis samples could appear to contain too much $^{3}He_{ET}$ if the two-component assumption used to calculate $^{3}He_{ET}$ concentrations is invalid. This could occur if mantle helium, bearing a $^{3}He/^{4}He$ ratio ~8 R_A at mid-ocean ridges (Graham, 2002), comprised a significant fraction of total sample helium and consequently inflated $^{3}He_{ET}$ concentration estimates.

Hydrothermal vents emit mantle helium that can be trapped within sulfide precipitates at the vent site itself (Jean-Baptiste and Fouquet, 1996; Stuart et al., 1994). If the $^{3}He_{ET}$ concentrations calculated for the nearest-axis Juan de Fuca Ridge and Mid-Atlantic Ridge samples were significantly biased by the presence of sulfide hosted mantle helium, then sedimentary $^{230}Th_{XS}/^{3}He_{ET}$ ratios should exhibit a negative correlation with high concentrations of hydrothermal material. However, no significant correlations are observed between $^{230}Th_{XS}/^{3}He_{ET}$ and Fe_{HT} or Cu_{HT} concentrations in either GGC3 ($R^2_{Fe} = 0.02$, p = 0.37; $R^2_{Cu} = .02$, p = 0.36), GGC6 ($R^2_{Fe} = 0.00$, p = 0.36; $R^2_{Cu} = 0.08$, p = 0.10), or 12PC ($R^2_{Fe} = 0.21$, p = 0.06; $R^2_{Cu} = 0.22$, p = 0.06; Supplemental Figure S4).

The presence of mantle helium bound in sedimentary basalt fragments could also lead to an apparent surplus in $^{3}He_{ET}$. Yet, this potential effect does not appear to be significant in 12PC because the sedimentary interval with the highest occurrence of basalt chips (>545 ka, Ferguson et al., 2017) is also the interval yielding some of the lowest concentrations of $^{3}He_{ET}$ in the record. The absence of systematic $^{3}He_{ET}$ offsets between 12PC sample aliquots that were sieved to eliminate basalt fragments and unsieved aliquots further suggests that basalt helium is not a significant contributor to the sedimentary ^{3}He measured in this study (Section 2.2). The 12PC data are consistent with previous work on GGC3, in which basalt contributions to sample estimates of $^{3}He_{ET}$ were also found to be minimal (Middleton et al., 2016). From these observations, we conclude that the $^{3}He_{ET}$ measurements in this study are not significantly biased by the mid-ocean ridge depositional environment.

The near-axis $^{230}Th_{XS}/^{3}He_{ET}$ anomalies cannot easily be explained by potential fractionation of the $^{3}He_{ET}$ and $^{230}Th_{XS}$ carrier phases during lateral sediment transport processes, either. At the Mid-Atlantic Ridge, temporal variations in $^{230}Th_{XS}/^{3}He_{ET}$ values are relatively synchronous over at least the past 35 ka, while temporal variations in GGC3 and GGC6 sediment focusing factors are quite distinct (Middleton et al., 2018; Figure 8). For example, the $^{3}He_{ET}$ -derived sediment focusing factor in GGC3 drops from ~4 to 2 across the minimum in Mid-Atlantic Ridge $^{230}Th_{XS}/^{3}He_{ET}$ values around 25 ka. Yet, the focusing factor in GGC6 increases from ~2 to 4 over the same interval. There is no clear pattern between sediment focusing and anomalous

^{230}Th$_{XS}$/^{3}He$_{ET}$ ratios in 12PC on the Juan de Fuca Ridge either. The lowest ^{230}Th$_{XS}$/^{3}He$_{ET}$ values in 12PC coincide with Marine Isotope Stage 11 (MIS 11; 374 to 424 ka), when the ^{3}He$_{ET}$-derived focusing factor indicates almost no lateral sediment transport at all (Ψ_{He} = 0.93; Figure 8).

The geologic context of the examined study regions suggests that the low ^{230}Th$_{XS}$/^{3}He$_{ET}$ values observed in the nearest-axis samples result from complications in ^{230}Th$_{XS}$, not ^{3}He$_{ET}$. On the Juan de Fuca Ridge, for example, similarities between the ^{3}He$_{ET}$-derived accumulation rates in 12PC sediments older than 300 ka and the ^{230}Th$_{XS}$-derived accumulation rates from contemporaneous sediments in the neighboring SeaVOICE cores (Costa and McManus, 2017; Figure 9) suggest that ^{3}He$_{ET}$ behaves as a reliable orbital-scale constant flux proxy throughout the record. Further, on the Mid-Atlantic Ridge, temporal variability in ^{3}He$_{ET}$-derived GGC3 and GGC6 dust flux records matches expectations based on upwind records from the Northwest African Margin (Middleton et al., 2018; Skonieczny et al., 2019). Thus, although potential complications in ^{3}He$_{ET}$ systematics cannot be definitively ruled out, hydrothermal interactions with seawater ^{230}Th$_{XS}$ are the most likely explanation for the anomalous ^{230}Th$_{XS}$/^{3}He$_{ET}$ observed in these near-axis sediments.

4.3.2. Hydrothermal Scavenging and a Dearth of ^{230}Th$_{XS}$

The low ^{230}Th$_{XS}$/^{3}He$_{ET}$ values, suggestive of relatively low ^{230}Th$_{XS}$ deposition rates, observed in the nearest-axis Juan de Fuca Ridge and Mid-Atlantic Ridge sediments reflect ^{230}Th$_{XS}$ behavior *opposite* to the relatively high rates of ^{230}Th$_{XS}$ deposition recorded in sediment cores from 6°S to 19°S on the East Pacific Rise (Lund et al., 2019). Further, while variations in ^{230}Th$_{XS}$ deposition are well correlated with hydrothermal iron (Fe$_{HT}$) fluxes in the East Pacific Rise sediments (Figure 7b), such correlations between ^{230}Th$_{XS}$ and Fe$_{HT}$ fluxes are either weak or insignificant in the full records from the Juan de Fuca Ridge (R^2 = 0.34, p < 0.01 09PC, and R^2 = 0.06, p = 0.09 in 12PC) or the Mid-Atlantic Ridge (R^2 = 0.01, p = 0.39 GGC3, and R^2 = 0.02, p = 0.15 in GGC6). In a global comparison, the correlation between Fe$_{HT}$ and ^{230}Th$_{XS}$ fluxes appears to manifest in sediments with Fe$_{HT}$ fluxes exceeding ~10 to 20 mg/cm^2 kyr (Figure 7b). Indeed, the correlation between ^{230}Th$_{XS}$ and Fe$_{HT}$ fluxes on the Juan de Fuca Ridge is higher when exclusively evaluated for samples with Fe$_{HT}$ fluxes >10 mg/cm^2 kyr (R^2 = 0.65, p < 0.01 in 09PC, sample size too small in 12PC). Such threshold behavior may mark the transition from one form of hydrothermal scavenging systematics to another. We propose that the ^{3}He$_{ET}$-normalized ^{230}Th$_{XS}$ flux data from the Juan de Fuca Ridge and the Mid-Atlantic Ridge sediments are not inconsistent with observations from the East Pacific Rise, rather they reflect a necessary and complementary component of the systematics of hydrothermal scavenging of ^{230}Th$_{XS}$ (Figure 10), as predicted by Lund et al. (2019).

Very close to hydrothermal vent sites, high fluxes of precipitating manganese oxides and iron oxyhydroxides remove seawater ^{230}Th$_{XS}$ at a sufficient rate to deplete the overlying waters in ^{230}Th$_{XS}$ (Hayes et al., 2015; Pavia et al., 2018). This intense near-axis hydrothermal scavenging sets up a concentration gradient in seawater ^{230}Th$_{XS}$ that drives the transport of off-axis seawater ^{230}Th$_{XS}$ towards the ^{230}Th$_{XS}$-depleted axis region via isopycnal eddy diffusion. Consequently, the ^{230}Th$_{XS}$ deposition rate in near-axis sediments will be *higher* than the ^{230}Th$_{XS}$ production rate of the overlying water column (> 1 R$_P$; "surplus zone" in Figure 10a), as observed on the East Pacific Rise (German et al., 2002; Lund et al., 2019). In the surrounding region from which

14

seawater $^{230}Th_{XS}$ was diffusively lost to the ridge, $^{230}Th_{XS}$ deposition rates to the underlying sediments will be *lower* than the water column production rate (< 1 R_P; "deficit zone" in Figure 10a), as observed in the Mid-Atlantic Ridge (in GGC3 and GGC6) and the Juan de Fuca Ridge (in 12PC >300 ka). Within deficit zone sediments, $^{230}Th_{XS}$ deposition rates may be decoupled from Fe_{HT} and Cu_{HT} fluxes because local $^{230}Th_{XS}$-burial deficiencies are driven by distal (near-axis) hydrothermal scavenging intensity. At a sufficient far-field distance from the ridge axis, diffusive $^{230}Th_{XS}$ loss from the overlying water column is negligible and local $^{230}Th_{XS}$ deposition rates again match the water column production rate (= 1 R_P; "far-field" in Figure 10a), as observed in the >10 km off-axis sediments from the Juan de Fuca Ridge (09PC and 12PC <300 ka). Thus, the magnitude and sign of hydrothermally induced biases in $^{230}Th_{XS}$-derived mass accumulation rates is expected to vary at a single ridge segment as a function of distance from the source of hydrothermal activity.

Given the mechanism described above, we predict that Juan de Fuca Ridge sediments would begin to exhibit increasing rates of $^{230}Th_{XS}$ deposition at ever closer distances to the axial hydrothermal systems. Due to radioactive decay, $^{230}Th_{XS}$ data is not available in 12PC sediments deposited within 5 km of the ridge-axis. However, surplus $^{230}Th_{XS}$ deposition has been qualitatively observed on the Cleft Segment in GC88-6 samples deposited within ~2 km of the ridge axis (German et al., 1997). If the spatial footprint of hydrothermal scavenging on the Juan de Fuca Ridge has been relatively constant over time, then the magnitude of surplus zone $^{230}Th_{XS}$ enrichment may be estimated from the total $^{230}Th_{XS}$ depletion of deficit zone sediments observed in 12PC. A minimum deficit zone $^{230}Th_{XS}$ depletion is determined from the average $^{230}Th_{XS}/^3He_{ET}$ ratio of 12PC sediments deposited between 5 and 9 km of the ridge axis (0.34 R_P; Figure 5). Assuming the entirety of this deficit $^{230}Th_{XS}$ was deposited within 5 km of the ridge axis, surplus zone sediments are expected to contain an average $^{230}Th_{XS}/^3He_{ET}$ ratio of at least 3.7 R_P, with higher values expected in closest proximity to the vent site (e.g., Figure 10a). Such $^{230}Th_{XS}$ surpluses are similar to the highest values observed on the East Pacific Rise (German et al., 2002; Lund et al., 2019). We emphasize that the >3.7 R_P estimate is a tentative value, as the spatial footprint of hydrothermal scavenging should vary temporally with the intensity of hydrothermal activity. Future investigation of Cleft Segment sedimentary records within 5 km of the ridge may allow for a more complete characterization of the distinct sedimentary $^{230}Th_{XS}$ regimes resulting from hydrothermal scavenging at a single ridge environment.

Importantly, the assorted length scales over which hydrothermal scavenging influences $^{230}Th_{XS}$ systematics vary globally from ridge to ridge and temporally at a single segment. Such variations are likely governed by the distribution and intensity of on-axis hydrothermal activity (Figure 10b). For example, at a distance of 8 km from the super-fast-spreading Southern East Pacific Rise, OC73-3-20 records peak $^3He_{ET}$-derived Fe_{HT} fluxes in excess of 700 mg/cm^2 kyr that coincide with $^{230}Th_{XS}$ deposition rates 4 times *higher* than the water column production rate (Figure 7; Lund et al., 2019). At the same distance of 8 km from the intermediate-spreading Juan de Fuca Ridge, 12PC sediments typically record ^3He_E-derived Fe_{HT} fluxes lower than 45 mg/cm^2 kyr and $^{230}Th_{XS}$ deposition rates 2 to 3 times *lower* than the water column production rate (Figure 5; Figure 7). Even on the East Pacific Rise, the $^{230}Th_{XS}/^3He_{ET}$ ratios in OC73-3-20 sediments approach 1 R_P when hydrothermal deposition rates are low (Figure 7; Lund et al., 2019). In general, lower levels of hydrothermal activity drive smaller concentration gradients in seawater $^{230}Th_{XS}$ and result in smaller hydrothermal footprints in sedimentary $^{230}Th_{XS}$ (Figure 10b).

While this work focuses on axial venting at mid-ocean ridges, we expect similar scavenging systematics to influence $^{230}Th_{XS}$ deposition in any region where intense high temperature hydrothermal activity generates high levels of manganese oxide and iron oxyhydroxide precipitates. Such locations may include those surrounding seamounts, hot spot volcanoes, back-arc basins, and off-axis hydrothermal fields. Though the global distribution of off-axis high temperature hydrothermal fields is poorly constrained, such fields can be associated with ridge-proximal fault systems and magmatism occurring up to ~10 km from the axial spreading center (e.g., Rona et al., 1990; Melchert et al., 2008; Han et al., 2014). We encourage the inclusion of $^3He_{ET}$ analyses to characterize sedimentary records recovered within the vicinity of any potential hydrothermal activity. Notably, low temperature or alkaline hydrothermal systems, such as Lost City on the Mid-Atlantic Ridge (e.g., Kelley et al., 2001), emit chemically distinct hydrothermal fluids that are unlikely to exhibit similar influences on the surrounding $^{230}Th_{XS}$ systematics as the high temperature systems discussed here.

4.3.3. Complications within the Mid-Atlantic Ridge

Interpretation of $^{230}Th_{XS}$ systematics within the axial valley of the Mid-Atlantic Ridge is complicated by its unique bathymetry and oceanographic conditions. Though the TAG and Broken Spur segments are >350 km apart, they are connected by a contiguous valley bound by the Kane and Atlantis transform faults. Consequently, GGC3 and GGC6 sediments could potentially be influenced by a singular $^{230}Th_{XS}$-depletion mechanism within the axial valley that similarly affects both locations due to along-axis currents. Such a regional-scale mechanism may explain the apparent synchronization in Mid-Atlantic Ridge $^{230}Th_{XS}/^3He_{ET}$ ratios over the past 35 kyr, despite the differences in hydrothermal input recorded in each core (Section 3.1.2).

Lateral advection of $^{230}Th_{XS}$-depleted seawater generated by intense upstream hydrothermal activity could potentially drive synchronous $^{230}Th_{XS}/^3He_{ET}$ variability at both GGC3 and GGC6. On the East Pacific Rise, Pavia et al. (2018) calculate a 64-year detectable lifetime for hydrothermally induced anomalies in water column concentrations of $^{230}Th_{XS}$. Mooring data from the Broken Spur segment indicate average along-axis current speeds of ~2 cm/s and suggest that hydrothermally influenced waters from Broken Spur could be transported to the TAG segment in about 6 months (Murton et al., 1999). Thus, $^{230}Th_{XS}$-depleted deficit zone seawater from an upstream vent field could be advected to both GGC3 and GGC6 faster than the time required for it to reequilibrate to normal $^{230}Th_{XS}$ concentrations. If such $^{230}Th_{XS}$-depleted seawater replaced the original seawater $^{230}Th_{XS}$ overlying TAG and Broken Spur, then it would yield deficit $^{230}Th_{XS}$ deposition fluxes at these sites. The decoupling between $^{230}Th_{XS}$-depletion and Fe_{HT} deposition observed in deficit zone sediments (e.g., Figure 7) suggest that deficit zone seawater may not carry a strong particulate plume signal. As a result, the along-axis transport of $^{230}Th_{XS}$-depleted deficit zone seawater might not be readily detectable using traditional nephelometry techniques. However, along-axis advection would imply that the original seawater $^{230}Th_{XS}$ overlying TAG and Broken Spur, which may not have had any $^{230}Th_{XS}$ deficit, would also have been transported downstream. In this case, sediments deposited at the end of the advection pathway may receive $^{230}Th_{XS}$ inputs from both local and advected seawater and may consequently contain relatively high $^{230}Th_{XS}/^3He_{ET}$ ratios.

Bottom scavenging of seawater $^{230}Th_{XS}$ by particle-rich nepheloid layers along the rough bathymetry of the axial valley and its steep side walls could also drive low $^{230}Th_{XS}$ deposition rates within the Mid-Atlantic Ridge (e.g., Bacon and Rutgers van der Loeff, 1989; Hayes et al., 2015). In the abyssal ocean, bottom scavenging may reduce seawater $^{230}Th_{XS}$ concentrations by up to ~50% in the lowermost water column (Okubo et al., 2012). Side wall scavenging within the Mid-Atlantic Ridge could further deplete seawater $^{230}Th_{XS}$ concentrations and limit $^{230}Th_{XS}$ deposition to the sediments below. Regional-scale variations in current speed through the axial valley, perhaps associated with climate variability, may serve to modify the effect of sidewall scavenging on the axial $^{230}Th_{XS}$ budget and consequently drive synchronous changes at TAG and Broken Spur. If the observed GGC3 and GGC6 sedimentary $^{230}Th_{XS}$ deficits result from side wall scavenging, then sediments recovered from shallower side wall locations should exhibit relatively high $^{230}Th_{XS}/^3He_{ET}$ values.

Notably, downslope transport of shallow water sediments, associated with lower $^{230}Th_{XS}$ deposition rates, to the >3000 m depths of GGC3 and GGC6 cannot account for the magnitude of $^{230}Th_{XS}$ deficit observed. The majority of GGC3 and GGC6 sediments would need to originate from water depths of <1500 m in order to explain the Mid-Atlantic Ridge observations, in which more than half of the overlying water column $^{230}Th_{XS}$ is absent. Yet, the areal extent of such bathymetric highs is extremely limited at both the TAG and Broken Spur segments (Figure 1).

Alternatively, the apparent synchronization in Mid-Atlantic Ridge $^{230}Th_{XS}/^3He_{ET}$ ratios may simply result from coinciding variations in both the TAG and Broken Spur hydrothermal systems that are not evidenced in the GGC3 and GGC6 Fe_{HT} and Cu_{HT} flux records (Figure 2). Given the decoupling between $^{230}Th_{XS}/^3He_{ET}$ ratios and local Fe_{HT} fluxes observed on the Juan de Fuca Ridge, it is possible that diffusive seawater $^{230}Th_{XS}$ loss towards axial vents within the Mid-Atlantic Ridge could generate $^{230}Th_{XS}$ deficits in GGC3 and GGC6 sediments in the absence of synchronous changes in local Fe_{HT} fluxes (Section 4.1). The larger spatial footprint of hydrothermal scavenging on sedimentary $^{230}Th_{XS}$, relative to sedimentary Fe_{HT}, may also allow for diffusive $^{230}Th_{XS}$ loss over or around the bathymetric barrier at Broken Spur that shields GGC6 sediments from direct deposition of Fe_{HT} particles (e.g., Figure 1). Under these conditions, sedimentary $^{230}Th_{XS}/^3He_{ET}$ ratios may provide a more holistic record of hydrothermal variability than Fe_{HT} and Cu_{HT} flux records alone. This hypothesis could be tested by investigating sedimentary $^{230}Th_{XS}/^3He_{ET}$ records surrounding TAG and Broken Spur at higher spatial resolution. Coincident hydrothermal variability at multiple segments along the Mid-Atlantic Ridge may result by chance or by a larger driving mechanism, such as the potential relationship between sea level change and submarine hydrothermal activity (Costa et al., 2017; Lund et al., 2016; Lund and Asimow, 2011; Lund et al., 2019; Middleton et al., 2016).

5. Conclusions

Coupled $^3He_{ET}$-$^{230}Th_{XS}$ analyses allow for characterization of hydrothermal scavenging effects on $^{230}Th_{XS}$-derived mass accumulation rates in mid-ocean ridge sediment cores. Sedimentary $^{230}Th_{XS}/^3He_{ET}$ ratios in most samples from the Juan de Fuca Ridge indicate reasonably consistent behavior of both $^3He_{ET}$ and $^{230}Th_{XS}$ as constant flux proxies. However, Juan de Fuca Ridge sediments deposited <10 km from the ridge-axis and both Mid-Atlantic Ridge records exhibit average $^{230}Th_{XS}/^3He_{ET}$ ratios that are less than half the local production ratio, suggesting

significant sedimentary $^{230}Th_{XS}$ deficits in these near-axis samples. Across the global ridge system, $^{3}He_{ET}$-derived $^{230}Th_{XS}$ deposition data indicate that the spatial footprint of hydrothermal scavenging varies globally and temporally, likely associated with variations in the intensity of local hydrothermal activity.

Within the hydrothermal footprint, surplus zone sediments, located closest to the vent, exhibit relatively high $^{230}Th_{XS}$ deposition rates (and anomalously low $^{230}Th_{XS}$-derived mass accumulation rates) due to seawater $^{230}Th_{XS}$ scavenging onto hydrothermal precipitates. The surplus zone can extend off axis from <5 km on the Juan de Fuca Ridge and the Mid-Atlantic Ridge to >28 km on the East Pacific Rise (Lund et al., 2019). Surrounding the surplus zone, deficit zone sediments exhibit relatively low $^{230}Th_{XS}$ deposition rates (and anomalously high $^{230}Th_{XS}$-derived mass accumulation rates) due to diffusive loss of overlying seawater $^{230}Th_{XS}$ towards the $^{230}Th_{XS}$-depleted waters closest to the vent. Variations in the $^{230}Th_{XS}$ deposition rates of deficit zone sediments may be decoupled from that of metalliferous hydrothermal precipitates at the same location. On the Juan de Fuca Ridge, the deficit zone appears to extend <10 km off-axis.

Beyond the deficit zone, far-field sediments experience $^{230}Th_{XS}$ deposition rates equal to the water column production rate, enabling reliable utilization of $^{230}Th_{XS}$ as a constant flux proxy. However, we suggest caution when interpreting $^{230}Th_{XS}$-derived mass accumulation rate records from within the axial valley of slow spreading ridges. The unique morphology of these axial valleys can drive along-axis currents and boundary scavenging that may additionally complicate $^{230}Th_{XS}$ systematics, as observed in the Mid-Atlantic Ridge samples. We recommend more coupled $^{3}He_{ET}$-$^{230}Th_{XS}$ investigations of near-ridge sediments in order to further characterize the nature of hydrothermal scavenging and to evaluate the sedimentary $^{230}Th_{XS}/^{3}He_{ET}$ ratio as a paleo-proxy for segment-scale variations in hydrothermal activity.

Acknowledgements

Figure Captions

Figure 1: Locations of sediment cores examined in this work (circles). Study regions on the Mid-Atlantic Ridge (MAR; KN207-2-GGC3 and KN207-2-GGC6) and the Juan de Fuca Ridge (JdFR; AT26-19-09PC and AT26-19-12PC) are highlighted in insets. Diamonds indicate known locations of active (pink) and inactive (yellow) hydrothermal vent fields (Beaulieu et al., 2013). Dashed line depicts position of the Cleft Segment spreading axis. Locations of additional SeaVOICE cores (AT26-19-05PC, -35PC, -38PC, -39BB; triangles; Costa and McManus, 2017) and GC88-6 (pentagon; German et al., 1997) on the Cleft Segment of the Juan de Fuca Ridge, as well as Y71-09-106, Y71-07-49, and OC73-3-20 on the East Pacific Rise (EPR; Lund et al.,

2019) are also indicated for reference. Bathymetric contours are spaced at 400 m intervals. Global map and insets generated in GeoMapApp.

Figure 2: Comparison of hydrothermal fluxes in Mid-Atlantic Ridge sediments. a) Hydrothermal iron (Fe_{HT}) and b) hydrothermal copper (Cu_{HT}) fluxes for GGC6 (Broken Spur Segment, 29°N; open triangles) and GGC3 (TAG Segment, 26°N, closed triangles; Middleton et al. 2016). Insets highlight GGC6 flux records on a zoomed-in y-axis. GGC6 symbols and error bars excluded from insets for clarity. Low GGC6 Fe_{HT} and Cu_{HT} fluxes suggest weak hydrothermal deposition. Negative values reflect uncertainty in the lithogenic correction applied.

Figure 3: Mass accumulation rate records derived using $^{3}He_{ET}$ (open circles) and $^{230}Th_{XS}$ (gray squares) for sediments from a,b) the Mid-Atlantic Ridge (MAR; GGC3 and GGC6) and c,d) the Juan de Fuca Ridge (JdFR; 09PC and 12PC).

Figure 4: Sedimentary $^{230}Th_{XS}/^{3}He_{ET}$ records for a) the Mid-Atlantic Ridge (MAR; GGC3 and GGC6) and b) the Juan de Fuca Ridge (JdFR; 09PC and 12PC). Absolute ratios have been divided by the local production ratio (R_P) to allow for comparison between sites of different depths. Mid-Atlantic Ridge $^{230}Th_{XS}/^{3}He_{ET}$ values are consistently lower than the expected production ratio (1 R_P). On the Juan de Fuca Ridge, 12PC $^{230}Th_{XS}/^{3}He_{ET}$ values are increasingly lower than the production ratio with depth after ~300 ka. Note the change in axes scales between panels.

Figure 5: Juan de Fuca Ridge (JdFR; 09PC, 12PC) $^{230}Th_{XS}/^{3}He_{ET}$ values as a function of distance to the spreading axis of the nearby mid-ocean ridge. Absolute ratios have been divided by the local production ratio (R_P) to allow for comparison between sites of different depths. Paleo-distance is estimated assuming a Cleft Segment half-spreading rate of 30 mm/yr (Govers et al., 2001). Juan de Fuca Ridge $^{230}Th_{XS}/^{3}He_{ET}$ values decrease with increasing proximity to the ridge. Ratios are plotted on a log scale to highlight deviations from the production value of 1 R_P.

Figure 6: Global compilation of core-averaged sedimentary $^{230}Th_{XS}/^{3}He_{ET}$ ratios with 1 standard deviation about each mean. Absolute ratios have been divided by the local production ratio (R_P) to allow for comparison between sites of different depths. Cores retrieved in proximity to the Juan de Fuca Ridge (JdFR), the Mid-Atlantic Ridge (MAR), and the East Pacific Rise (EPR; Lund et al., 2019) are highlighted with colored symbols. Off-axis data from Serno et al. (2015), McGee et al. (2010), and Marcantonio et al. (1995, 1996, 1999, 2001a, 2001b). Ratios are plotted on a log scale to highlight deviations from the production value of 1 R_P.

Figure 7: Relationships between $^{3}He_{ET}$-derived $^{230}Th_{XS}$ fluxes and a) distance to the ridge-axis at time of deposition and b) $^{3}He_{ET}$-derived hydrothermal iron (Fe_{HT}) fluxes for sediments from the Mid-Atlantic Ridge (MAR; GGC3, GGC6), the Juan de Fuca Ridge (JdFR; 09PC, 12PC), and the East Pacific Rise (EPR; OC73-3-20, Y71-09-106, Y71-07-49; Lund et al., 2019). Fe_{HT} fluxes are calculated using $^{3}He_{ET}$-derived mass accumulation rates. Absolute $^{3}He_{ET}$-derived $^{230}Th_{XS}$ fluxes have been divided by the local $^{230}Th_{XS}$ production rate (R_P) to allow for comparison between sites of different depths. For consistency of comparison, $^{3}He_{ET}$-derived fluxes in East Pacific Rise records have been recalculated using a $^{3}He_{ET}$ influx of $8.0 \pm 1.2 \times 10^{-13}$ cc STP cm^{-2} kyr^{-1}. GGC6 samples with negative Fe_{HT} flux values are excluded from b.

19

Figure 8: $^3He_{ET}$-derived sediment focusing factors (dashed lines) and average $^{230}Th_{XS}/^3He_{ET}$ values between age model tie points (solid lines) for near-axis sediments from a) the Mid-Atlantic Ridge (MAR; GGC3, GGC6) and b) the Juan de Fuca Ridge (JdFR; 12PC). Absolute $^{230}Th_{XS}/^3He_{ET}$ ratios have been divided by the local production ratio (R_p). c) Direct comparison of $^{230}Th_{XS}/^3He_{ET}$ and focusing factor for GGC3 (closed triangles), GGC6 (open triangles), and 12PC (open circles). There are no clear relationships between sediment focusing and $^{230}Th_{XS}/^3He_{ET}$ variability.

Figure 9: Comparison of $^3He_{ET}$-derived (open circles) and $^{230}Th_{XS}$ -derived (black line) mass accumulation rates from 12PC on the Juan de Fuca Ridge with $^{230}Th_{XS}$-derived mass accumulation rates of neighboring SeaVOICE cores (05PC, 09PC, 35PC, 38PC, 39BB; color lines; Costa and McManus, 2017). In sediments older than 300 ka, $^{230}Th_{XS}$-derived mass accumulation rates are significantly higher in 12PC than in neighboring cores, but $^3He_{ET}$-derived values from 12PC are not. SeaVOICE core locations are indicated in Figure 1.

Figure 10: Conceptual diagram illustrating the variable effects of hydrothermal scavenging of seawater $^{230}Th_{XS}$ on $^{230}Th_{XS}$ deposition rates in near-ridge sediments. a) Closest to the vent, $^{230}Th_{XS}$ deposition rates to surplus zone sediments are higher than the overlying water column production rate (R_P); farther from the vent site, $^{230}Th_{XS}$ deposition rates to deficit zone sediments are lower than the overlying water column production rate; beyond the footprint of hydrothermal influence, $^{230}Th_{XS}$ deposition rates in far-field sediments match the water column production rate. b) Higher levels of hydrothermal Fe (Fe_{HT}) output at the vent site drive enhanced hydrothermal scavenging and result in a larger hydrothermal footprint in sedimentary $^{230}Th_{XS}$.

References

Adkins, J., Demenocal, P. and Eshel, G. (2006) The "African humid period" and the record of marine upwelling from excess 230Th in Ocean Drilling Program Hole 658C. *Paleoceanography* **21**.

Andersen, M., Stirling, C., Zimmermann, B. and Halliday, A.N. (2010) Precise determination of the open ocean 234U/238U composition. *Geochemistry, Geophysics, Geosystems* **11**, Q12003.

Anderson, R., Ali, S., Bradtmiller, L., Nielsen, S., Fleisher, M., Anderson, B. and Burckle, L. (2009) Wind-driven upwelling in the Southern Ocean and the deglacial rise in atmospheric CO2. *Science* **323**, 1443-1448.

Auffret, G.A., Richter, T., Reyss, J.L., Organo, C., Deloule, E., Gaillard, J.F., Dennielou, B., Muller, C., Thomas, B., Watremez, P., Grousset, F., Boelaert, A., Cambon, P. and Etoubleau, J. (1996) Record of hydrothermal activity in sediments from the Mid-Atlantic Ridge south of the Azores. *C. R. Acad. Sci.* **323**, 583-590.

Bacon, M.P. (1984) Glacial to interglacial changes in carbonate and clay sedimentation in the Atlantic Ocean estimated from 230Th measurements. *Chemical Geology* **46**, 97-111.

Bacon, M.P. and Anderson, R.F. (1982) Distribution of thorium isotopes between dissolved and particulate forms in the deep sea. *Journal of Geophysical Research* **87**, 2045-2056.

Bacon, M.P. and Rutgers van der Loeff, M.M. (1989) Removal of thorium-234 by scavenging in the bottom nepheloid layer of the ocean. *Earth and Planetary Science Letters* **92**, 157-164.

Baker, E.T. and German, C.R. (2004) On the global distribution of hydrothermal vent fields, in: German, C.R., Lin, J., Parson, L.M. (Eds.), *Mid-Ocean Ridges: Hydrothermal Interactions between the Lithosphere and Oceans*, pp. 245-266.

Beaulieu, S.E., Baker, E.T., German, C.R. and Maffei, A. (2013) An authoritative global database for active submarine hydrothermal vent fields. *Geochemistry Geophysics Geosystems* **14**, 4892-4905.

Castillo, S., Moreno, T., Querol, X., Alastuey, A., Cuevas, E., Herrmann, L., Mounkaila, M. and Gibbons, W. (2008) Trace element variation in size-fractionated African desert dusts. *Journal of Arid Environments* **72**, 1034-1045.

Cave, R.R., German, C.R., Thomson, J. and Nesbitt, R.W. (2002) Fluxes to sediments underlying the Rainbow hydrothermal plume at 36o14'N on the Mid-Atlantic Ridge. *Geochim. Cosmochim. Acta.* **66**, 1905-1923.

Cherkashev, G. (1995) Hydrothermal input into sediments of the Mid-Atlantic Ridge. *Geol. Soc. London Sp.* **87**, 223-229.

Costa, K. and McManus, J. (2017) Efficacy of 230Th normalization in sediments from the Juan de Fuca Ridge, northeast Pacific Ocean. *Geochimica Et Cosmochimica Acta* **197**, 215-225.

Costa, K., McManus, J., Boulahanis, B., Carbotte, S., Winckler, G., Huybers, P.J. and Langmuir, C.H. (2016a) Sedimentation, stratigraphy and physical properties of sediment on the Juan de Fuca Ridge. *Marine Geology* **380**, 163-173.

Costa, K.M., McManus, J.F., Anderson, R.F., Ren, H., Sigman, D., Winckler, G., Fleisher, M.Q., Marcantonio, F. and Ravelo, A.C. (2016b) No iron fertilization in the equatorial Pacific Ocean during the last ice age. *Nature* **529**, 519.

Costa, K.M., McManus, J.F., Middleton, J.L., Langmuir, C.H., Huybers, P.J., Winckler, G., Mukhopadhyay, S.J.E. and Letters, P.S. (2017) Hydrothermal deposition on the Juan de Fuca Ridge over multiple glacial–interglacial cycles. *Earth and Planetary Science Letters* **479**, 120-132.

Crowley, J.W., Katz, R.F., Huybers, P., Langmuir, C.H. and Park, S.-H. (2015) Glacial cycles drive variations in the production of oceanic crust. *Science* **347**, 1237-1240.

Farley, K., Love, S. and Patterson, D. (1997) Atmospheric entry heating and helium retentivity of interplanetary dust particles. *Geochim. Cosmochim. Acta.* **61**, 2309-2316.

Farley, K.A. (1995) Cenozoic variations in the flux of interplanetary dust recorded by 3He in a deep-sea sediment. *Nature* **376**, 153-156.

Farley, K.A. and Patterson, D.B. (1995) A 100-kyr periodicity in the flux of extraterrestrial 3He to the sea floor. *Nature* **378**, 600-603.

Ferguson, D.J., Li, Y., Langmuir, C.H., Costa, K.M., McManus, J.F., Huybers, P. and Carbotte, S.M. (2017) A 65 ky time series from sediment-hosted glasses reveals rapid transitions in ocean ridge magmas. *Geology* **45**, 491-494.

Fleisher, M. and Anderson, R. (2003) Assessing the collection efficiency of Ross Sea sediment traps using 230Th and 231Pa. *Deep Sea Research Part II: Topical Studies in Oceanography* **50**, 693-712.

Francois, R., Frank, M., Rutgers van der Loeff, M.M. and Bacon, M.P. (2004) 230Th normalization: An essential tool for interpreting sedimentary fluxes during the late Quaternary. *Paleoceanography* **19**.

Frank, M., Eckhardt, J.-D., Eisenhauer, A., Kubik, P.W., Dittrich-Hannen, B., Segl, M. and Mangini, A. (1994) Beryllium 10, thorium 230, and protactinium 231 in Galapagos microplate sediments: Implications of hydrothermal activity and paleoproductivity changes during the last 100,000 years. *Paleoceanography* **9**, 559-578.

Gale, A., Dalton, C.A., Langmuir, C.H., Su, Y., Schilling, J.-G. (2013) The mean composition of ocean ridge basalts. *Geochemistry, Geophysics, Geosystems* **14**, 489-518.

German, C., Colley, S., Palmer, M., Khripounoff, A. and Klinkhammer, G. (2002) Hydrothermal plume-particle fluxes at 13 N on the East Pacific Rise. *Deep Sea Research Part I: Oceanographic Research Papers* **49**, 1921-1940.

German, C. and Sparks, R. (1993) Particle recycling in the TAG hydrothermal plume. *Earth and Planetary Science Letters* **116**, 129-134.

German, C.R., Bourles, D.L., Brown, E.T., Hergt, J., Colley, S., Higgs, N.C., Ludford, E.M., Nelsen, T.A., Feely, R.A., Raisbeck, G. and Yiou, F. (1997) Hydrothermal scavenging on the Juan de Fuca Ridge: Th-230(xs), Be-10, and REEs in ridge-flank sediments. *Geochim. Cosmochim. Acta.* **61**, 4067-4078.

German, C.R., Rudnicki, M.D. and Klinkhammer, G.P. (1999) A segment-scale survey of the Broken Spur hydrothermal plume. *Deep-Sea Res. Pt. I* **46**, 701-714.

Govers, R. and Meijer, P.T. (2001) On the dynamics of the Juan de Fuca plate. *Earth and Planetary Science Letters* **189**, 115-131.

Graham, D.W. (2002) Noble gas isotope geochemistry of mid-ocean ridge and ocean island basalts: Characterization of mantle source reservoirs. *Rev. Mineral Geochem.* **47**, 247-318.

Han, S., Carbotte, S.M., Carton, H., Mutter, J.C., Aghaei, O., Nedimovic, M.R., and Canales, J.P. (2014) Architecture of on- and off-axis magma bodies at EPR 9°37-40'N and implications for oceanic crustal accretion. *Earth and Planetary Science Letters* **390**, 31-44.

Haug, G.H., Sigman, D.M., Tiedemann, R., Pedersen, T.F. and Sarnthein, M. (1999) Onset of permanent stratification in the subarctic Pacific Ocean. *Nature* **401**, 779.

Hayes, C.T., McGee, D., Mukhopadhyay, S., Boyle, E.A., and Maloof, A.C. (2017) Helium and thorium isotope constraints on African dust transport to the Bahamas over recent millennia. *Earth and Planetary Science Letters* **457**, 385-394.

Hayes, C.T., Anderson, R.F., Fleisher, M.Q., Huang, K.-F., Robinson, L.F., Lu, Y., Cheng, H., Edwards, R.L. and Moran, S.B. (2015) 230Th and 231Pa on GEOTRACES GA03, the US GEOTRACES North Atlantic transect, and implications for modern and paleoceanographic chemical fluxes. *Deep Sea Research Part II: Topical Studies in Oceanography* **116**, 29-41.

Henderson, G.M., Anderson, R.F. and Geochemistry (2003) The U-series toolbox for paleoceanography. *Reviews in Mineralogy and Geochemistry* **52**, 493-531.

Higgins, S.M., Anderson, R.F., Marcantonio, F., Schlosser, P. and Stute, M. (2002) Sediment focusing creates 100-ka cycles in interplanetary dust accumulation on the Ontong Java Plateau. *Earth and Planetary Science Letters* **203**, 383-397.

Humphris, S.E. and Tivey, M.K. (2000) A synthesis of geological and geochemical investigations of the TAG hydrothermal field: Insights into fluid-flow and mixing
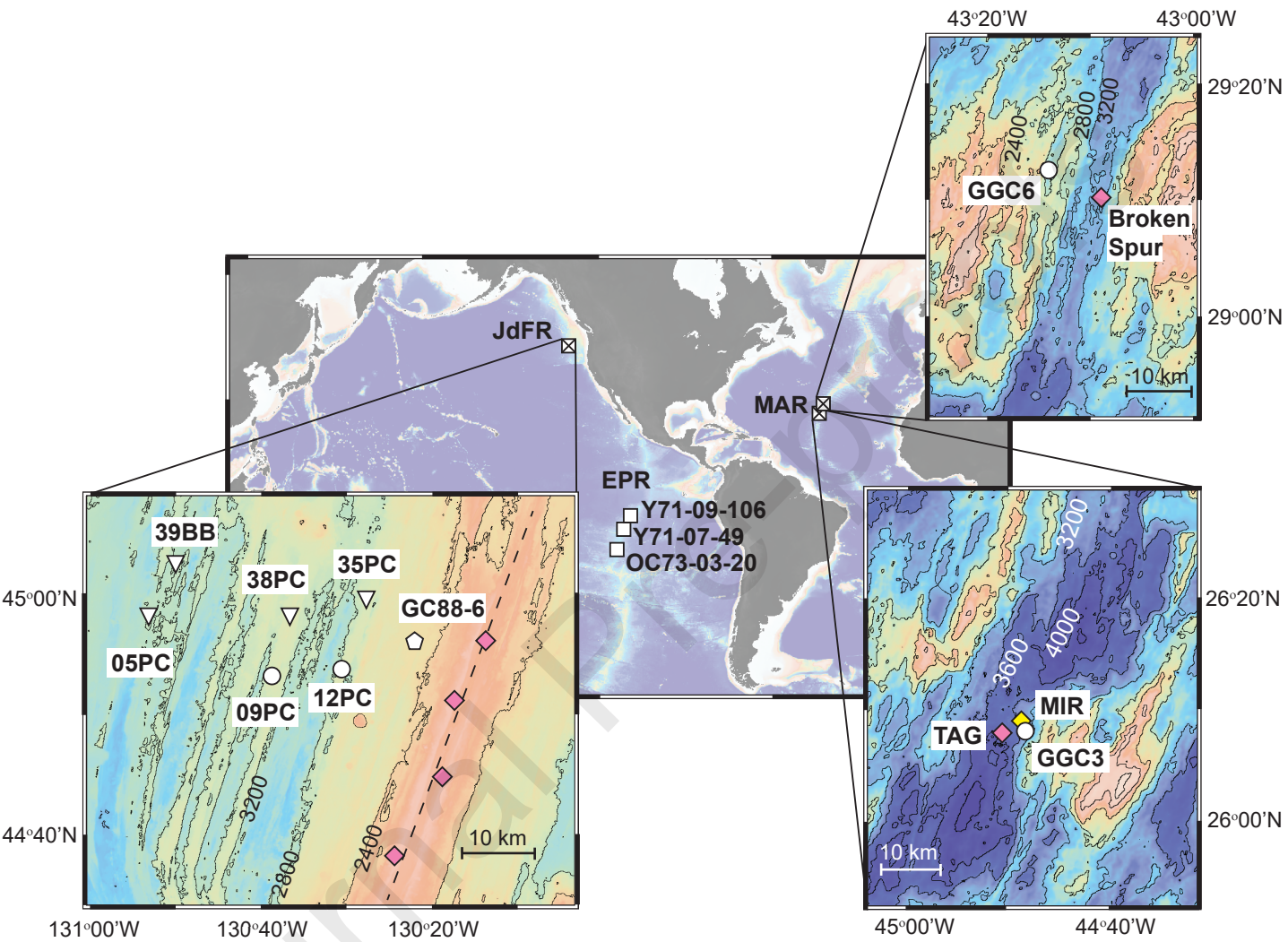
processes in a hydrothermal system. *Geological Society of America Special Papers*, 213-236.

Huybers, P. and Langmuir, C. (2009) Feedback between deglaciation, volcanism, and atmospheric CO2. *Earth Planet. Sci. Lett.* **286**, 479-491.

Jean-Baptiste, P. and Fouquet, Y. (1996) Abundance and isotopic composition of helium in hydrothermal sulfides from the East Pacific Rise at 13°N. *Geochim. Cosmochim. Acta* **60**, 87-93.

Kelley, D.S., Karson, J.A., Blackman, D.K., Früh-Green, G.L., Butterfield, D.A., Lilley, M.D., Olson, E.J., Schrenk, M.O., Roe, K.K., Lebon, G.T., Rivizzigno, P., and the AT3-60 Shipboard Party (2001) An off-axis hydrothermal vent field near the Mid-Atlantic Ridge at 30°N. *Nature* **412**, 145-149.

Lund, D., Asimow, P., Farley, K., Rooney, T., Seeley, E., Jackson, E. and Durham, Z. (2016) Enhanced East Pacific Rise hydrothermal activity during the last two glacial terminations. *Science* **351**, 478-482.

Lund, D.C. and Asimow, P.D. (2011) Does sea level influence mid-ocean ridge magmatism on Milankovitch timescales? *Geochem. Geophys. Geosyst*. **12.**

Lund, D.C., Pavia, F.J., Seeley, E.I., McCart, S.E., Rafter, P.A., Farley, K.A., Asimow, P.D. and Anderson, R.F. (2019) Hydrothermal scavenging of 230Th on the Southern East Pacific Rise during the last deglaciation. *Earth and Planetary Science Letters* **510**, 64-72.

Marcantonio, F., Anderson, R.F., Higgins, S., Fleisher, M.Q., Stute, M. and Schlosser, P. (2001a) Abrupt intensification of the SW Indian Ocean monsoon during the last deglaciation: constraints from Th, Pa, and He isotopes. *Earth and Planetary Science Letters* **184**, 505-514.

Marcantonio, F., Anderson, R.F., Higgins, S., Stute, M., Schlosser, P. and Kubik, P. (2001b) Sediment focusing in the central equatorial Pacific Ocean. *Paleoceanography* **16**, 260-267.

Marcantonio, F., Anderson, R.F., Stute, M., Kumar, N., Schlosser, P. and Mix, A. (1996) Extraterrestrial 3He as a tracer of marine sediment transport and accumulation. *Nature* **383**, 705-707.

Marcantonio, F., Higgins, S., Anderson, R.F., Stute, M., Schlosser, P. and Rasbury, E.T. (1998) Terrigenous helium in deep-sea sediments. *Geochim. Cosmochim. Acta* **62**, 1535-1543.

Marcantonio, F., Kumar, N., Stute, M., Anderson, R.F., Seidl, M.A., Schlosser, P. and Mix, A. (1995) A comparative study of accumulation rates derived by He and Th isotope analysis of marine sediments. *Earth Planet. Sci. Lett.* **133**, 549-555.

Marcantonio, F., Turekian, K.K., Higgins, S., Anderson, R.F., Stute, M. and Schlosser, P. (1999) The accretion rate of extraterrestrial 3He based on oceanic 230Th flux and the relation to Os isotope variation over the past 200,000 years in an Indian Ocean core. *Earth and Planetary Science Letters* **170**, 157-168.

McGee, D., Marcantonio, F., McManus, J.F., and Winckler, G. (2010) The response of excess 230Th and extraterrestrial 3He to sediment redistribution at the Blake Ridge, western North Atlantic. *Earth and Planetary Science Letters* **299**, 138-149.

McGee, D. and Mukhopadhyay, S. (2013) Extraterrestrial He in sediments: From recorder of asteroid collisions to timekeeper of global environmental changes, *The Noble Gases as Geochemical Tracers*. Springer-Verlag, Hiedelberg, Heidelberg, pp. 155-176.

McGregor, B.A. and Rona, P.A. (1975) Crest of the Mid-Atlantic Ridge at 26° N. *Journal of Geophysical Research* **80**, 3307-3314.
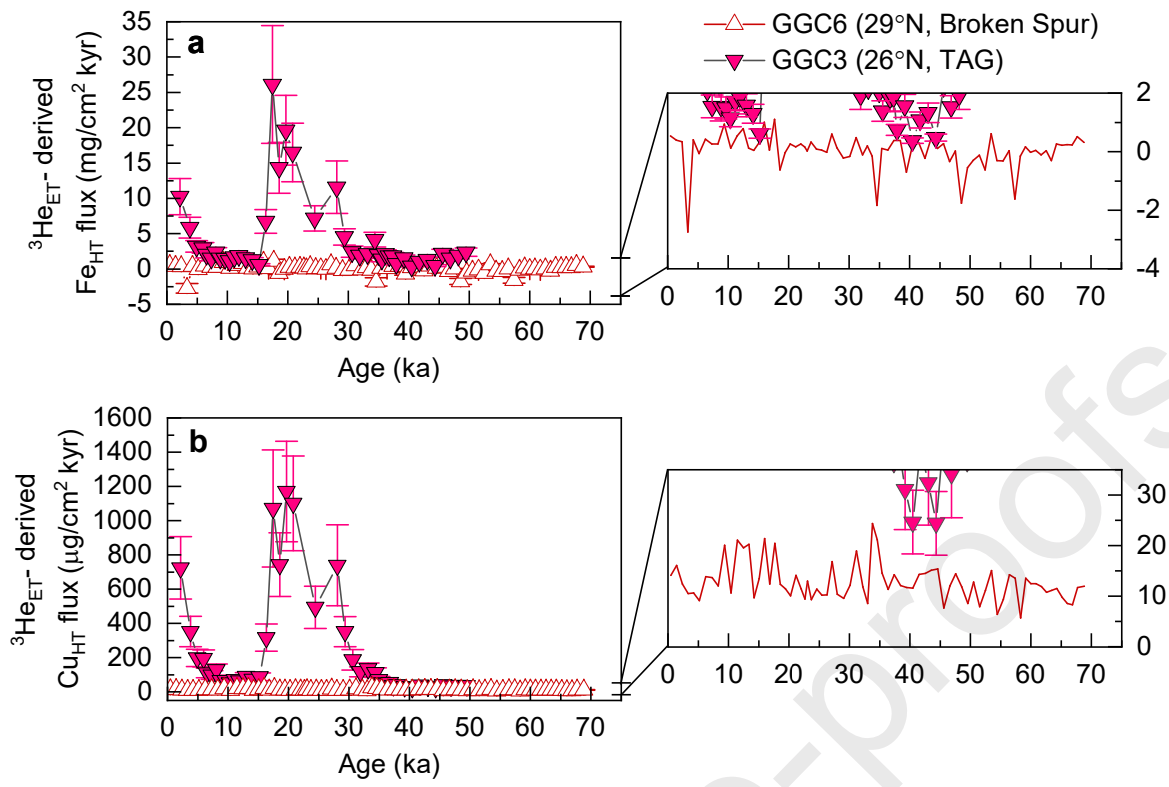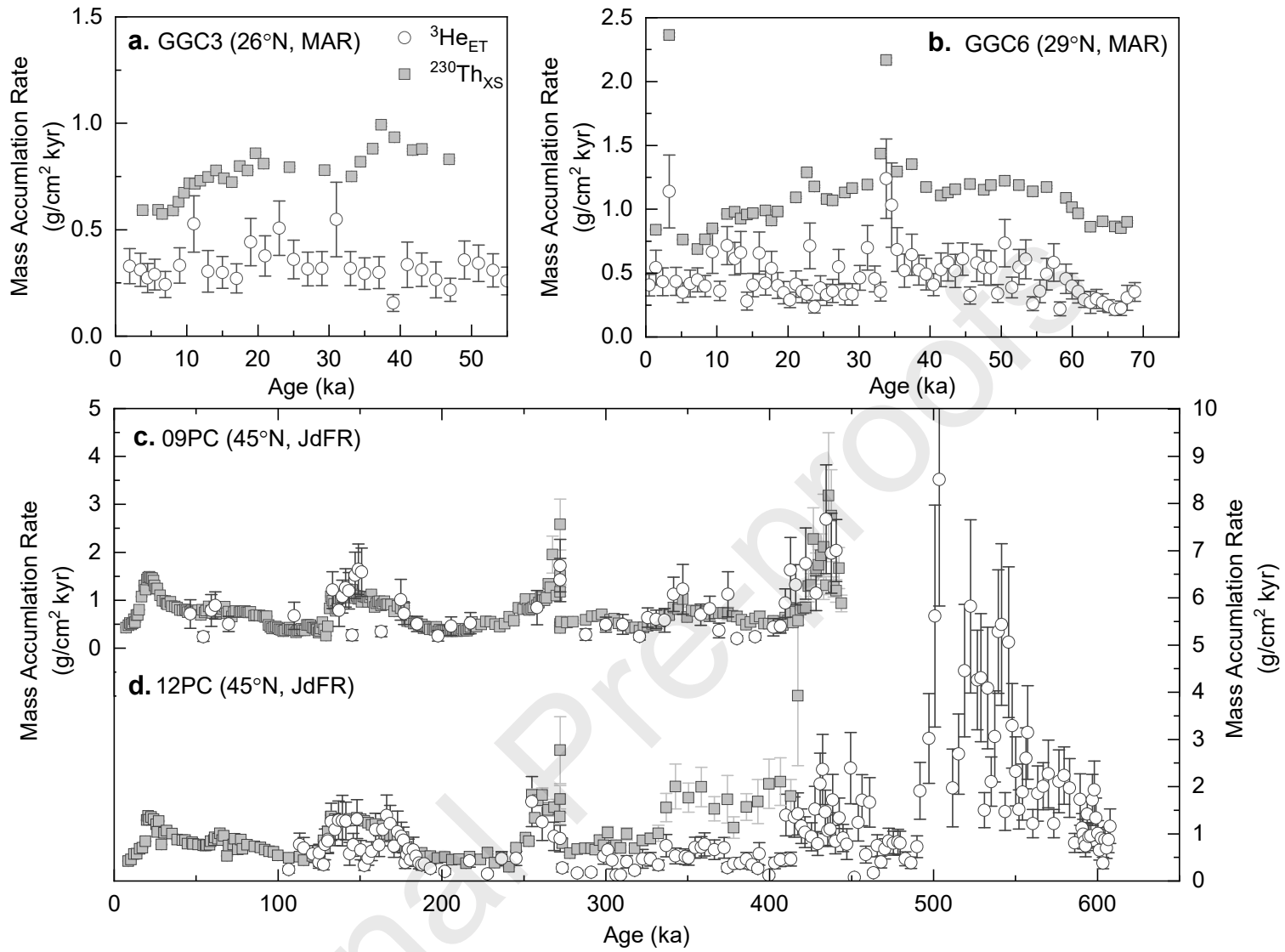
McManus, J.F., Anderson, R.F., Broecker, W.S., Fleisher, M.Q. and Higgins, S.M. (1998) Radiometrically determined sedimentary fluxes in the sub-polar North Atlantic during the last 140,000 years. *Earth and Planetary Science Letters* **155**, 29-43.

Melchert, B. Devey, C.W., German, C.R., Lackschewitz, K.S., Seifert, R., Walter, M., Mertens, C., Yoerger, D.R., Baker, E.T., Paulick, H., and Nakamura, K. (2008) First evidence for high-temperature off-axis venting of deep crustal/mantle heat: The Nibelungen hydrothermal field, southern Mid-Atlantic Ridge. *Earth and Planetary Science Letters* **275**, 61-69.

Middleton, J.L., Langmuir, C.H., Mukhopadhyay, S., McManus, J.F. and Mitrovica, J.X. (2016) Hydrothermal iron flux variability following rapid sea level changes. *Geophysical Research Letters* **43**, 3848-3856.

Middleton, J.L., Mukhopadhyay, S., Langmuir, C.H., McManus, J.F. and Huybers, P.J. (2018) Millennial-scale variations in dustiness recorded in Mid-Atlantic sediments from 0 to 70 ka. *Earth and Planetary Science Letters* **482,** 12-22.

Mukhopadhyay, S., Farley, K. and Montanari, A. (2001) A 35 Myr record of helium in pelagic limestones from Italy: implications for interplanetary dust accretion from the early Maastrichtian to the middle Eocene. *Geochimica Et Cosmochimica Acta* **65**, 653-669.

Murton, B.J., Klinkhammer, G., Becker, K., Briais, A., Edge, D., Hayward, N., Millard, N., Mitchell, I., Rouse, I. and Rudnicki, M. (1994) Direct evidence for the distribution and occurrence of hydrothermal activity between 27 N–30 N on the Mid-Atlantic Ridge. *Earth and Planetary Science Letters* **125**, 119-128.

Murton, B.J., Redbourn, L.J., German, C.R. and Baker, E.T. (1999) Sources and fluxes of hydrothermal heat, chemicals and biology within a segment of the Mid-Atlantic Ridge. *Earth and Planetary Science Letters* **171**, 301-317.

Nier, A. and Schlutter, D. (1992) Extraction of helium from individual interplanetary dust particles by step-heating. *Meteoritics* **27**, 166-173.

Nier, A. and Schlutter, D. (1993) The thermal history of interplanetary dust particles collected in the Earth's stratosphere. *Meteoritics* **28**, 675-681.

Okubo, A., Obata, H., Gamo, T. and Yamada, M. (2012) 230Th and 232Th distributions in mid-latitudes of the North Pacific Ocean: effect of bottom scavenging. *Earth and Planetary Science Letters* **339**, 139-150.

Patterson, D., Farley, K. and Schmitz, B. (1998) Preservation of extraterrestrial 3He in 480-Ma-old marine limestones. *Earth Planet. Sci. Lett.* **163**, 315-325.

Pavia, F., Anderson, R., Vivancos, S., Fleisher, M., Lam, P., Lu, Y., Cheng, H., Zhang, P. and Edwards, R.L. (2018) Intense hydrothermal scavenging of 230Th and 231Pa in the deep Southeast Pacific. *Marine Chemistry* **201**, 212-228.

Rona, P.A., Denlinger, R.P., Fisk, M.R., Howard, K.J., Taghon, G.L., Klitgord, K.d., McClain, J.S., McMurray, G.R., and Wiltshire, J.C. (1990) Major off-axis hydrothermal activity on the northern Gorda Ridge. *Geology* **18**, 493-496.

Ruddiman, W.F. (1997) Tropical Atlantic terrigenous fluxes since 25,000 yrs BP. *Marine Geology* **136**, 189-207.

Shimmield, G.B. and Price, N.B. (1988) The scavenging of U, Th-230 and Pa-231 during pulsed hydrothermal activity at 20S, East Pacific Rise. *Geochimica Et Cosmochimica Acta* **52**, 669-677.
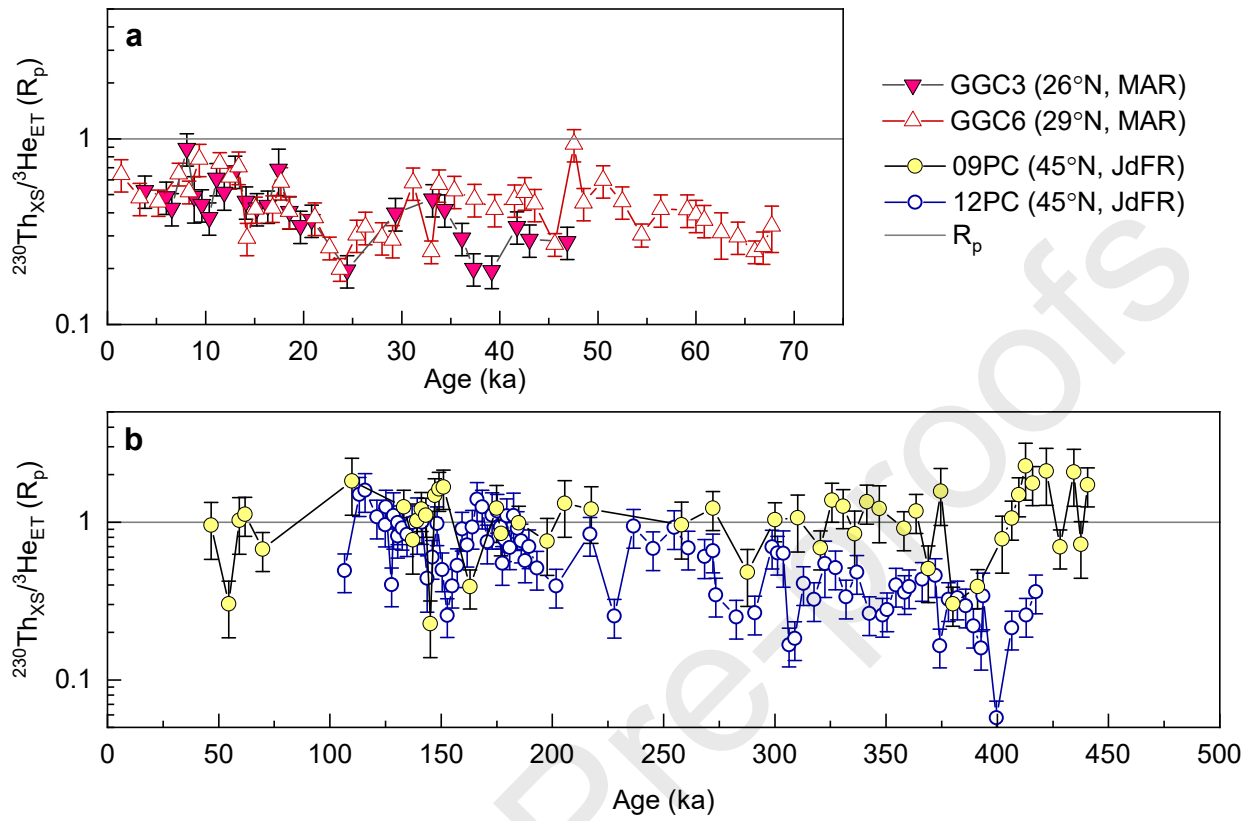
Skonieczny, C., McGee, D., Winckler, G., Bory, A., Bradtmiller, L., Kinsley, C., Polissar, P., De Pol-Holz, R., Rossignol, L. and Malaizé, B. (2019) Monsoon-driven Saharan dust variability over the past 240,000 years. *Science Advances* **5**, eaav1887.

Stuart, F., Turner, G., Duckworth, R.C. and Fallick, A. (1994) Helium isotopes as tracers of trapped hydrothermal fluids in ocean-floor sulfides. *Geology* **22**, 823-826.

Suman, D.O. and Bacon, M.P. (1989) Variations in Holocene sedimentation in the North-American Basin determined from Th-230 measurements. *Deep-Sea Research Part A-Oceanographic Research Papers* **36**, 869-878.

Takayanagi, M. and Ozima, M. (1987) Temporal variation of 3He/4He ratio recorded in deep-sea sediment cores. *J. Geophys. Res.* **92**, 12531-12538.

Taylor, S.R. and McLennan, S.M. (1995) The geochemical evolution of the continental crust. *Rev. Geophys.* **33**, 241-265.

Theiler, J., Eubank, S., Longtin, A., Galdrikian, B. and Farmer, J.D. (1992) Testing for nonlinearity in time series: the method of surrogate data. *Physica D: Nonlinear Phenomena* **58**, 77-94.

Tolstoy, M. (2015) Mid-ocean ridge eruptions as a climate valve. *Geophysical Research Letters* **42**, 1346-1351.

Valk, O., Rutgers van der Loeff, M., Geibert, W., Gdaniec, S., Rijkenberg, M.J., Moran, S.B., Lepore, K., Edwards, R., Lu, Y. and Puigcorbe, V. (2018) Importance of hydrothermal vents in scavenging removal of 230Th in the Nansen Basin. *Geophysical Research Letters* **45**, 10,539-510,548.

Winckler, G., Anderson, R.F., Fleisher, M.Q., McGee, D. and Mahowald, N. (2008) Covariant glacial-interglacial dust fluxes in the equatorial Pacific and Antarctica. *Science* **320**, 93-96.

Winckler, G., Anderson, R.F., Jaccard, S.L. and Marcantonio, F. (2016) Ocean dynamics, not dust, have controlled equatorial Pacific productivity over the past 500,000 years. *Proceedings of the National Academy of Sciences* **113**, 6119-6124.

Winckler, G., Anderson, R.F. and Schlosser, P. (2005) Equatorial Pacific productivity and dust flux during the mid-Pleistocene climate transition. *Paleoceanography* **20**, PA4025.
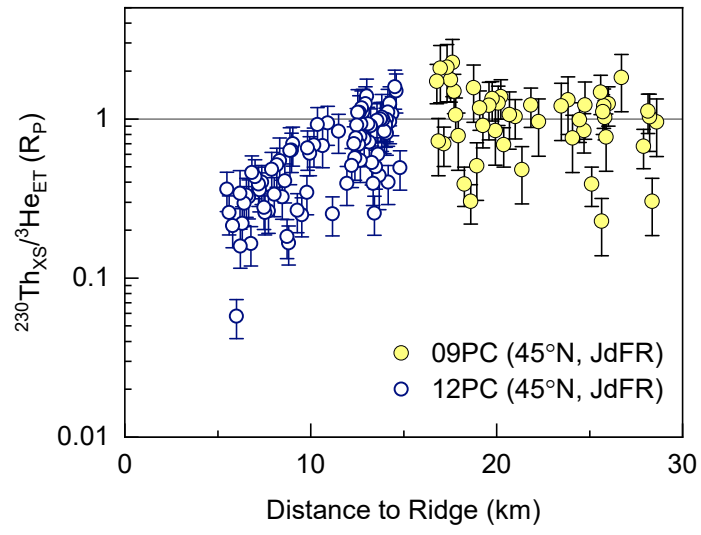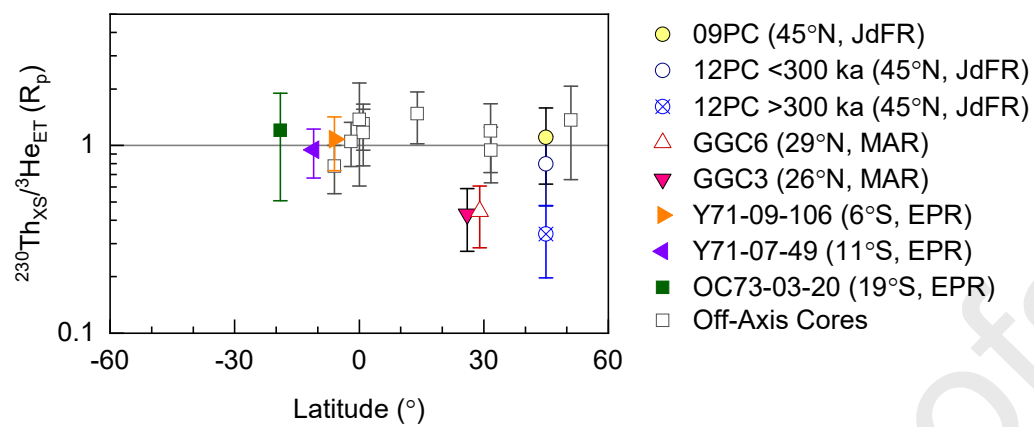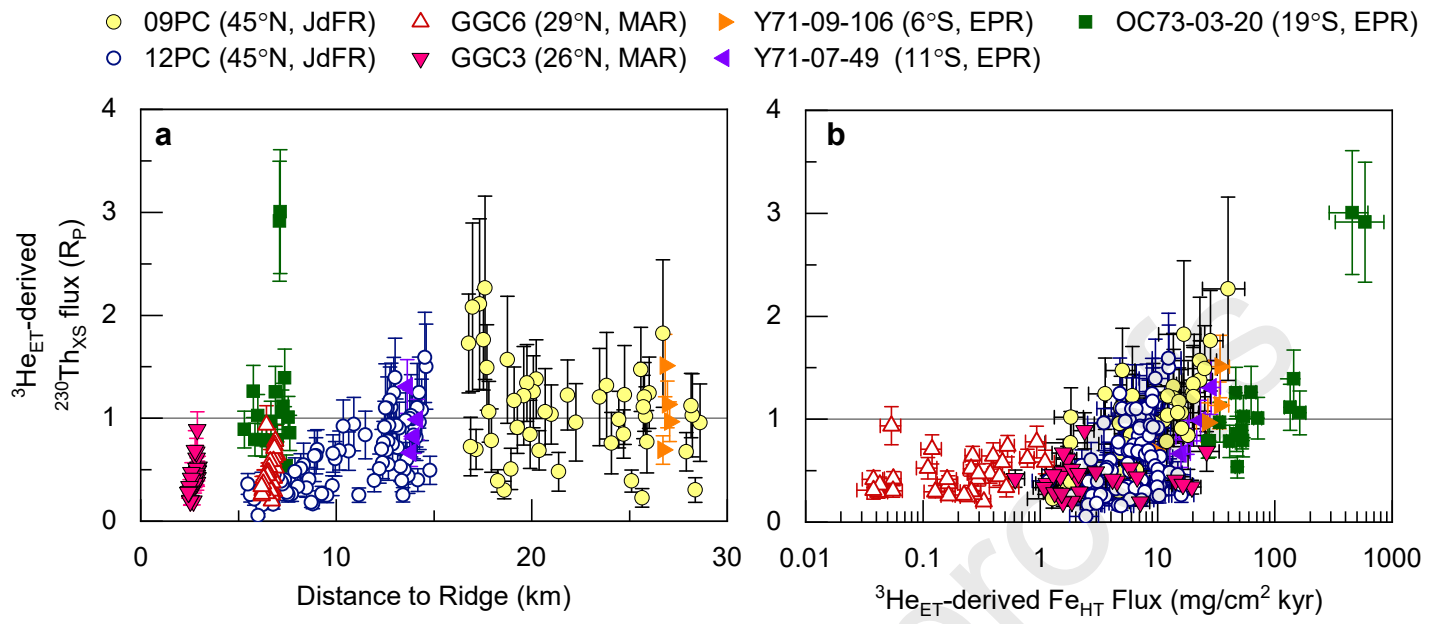
Figure 1

Figure2
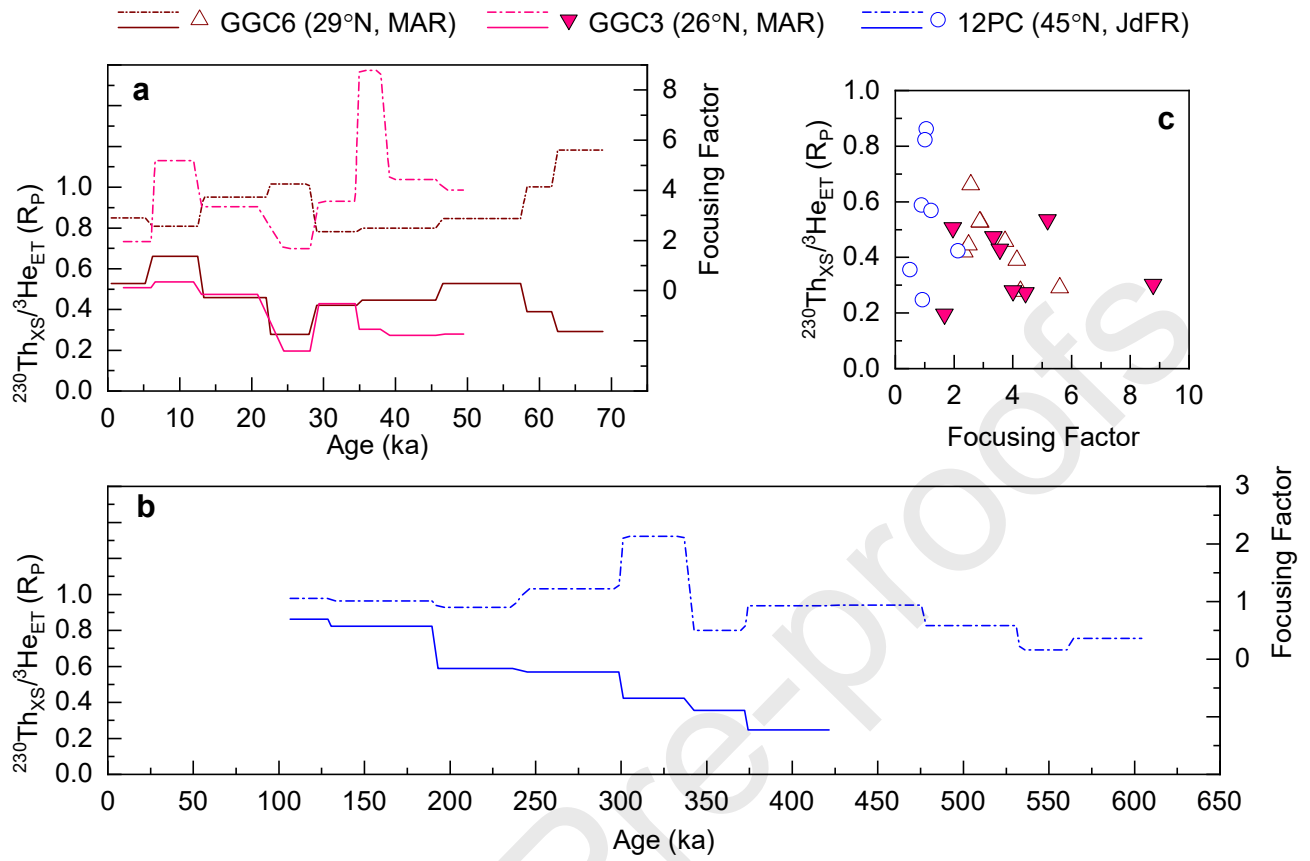
Figure3

Figure4

Figure5

Figure 6

Figure 7

Figure8

Figure9

Figure10

a.

Surplus Zone (> 1 R_P) Deficit Zone (< 1 R_P) Far-field (= 1 R_P)

$^{230}Th_{XS}$ Flux to Sediments (R_P)

1

Distance from Vent (km)

b.

footprint of hydothermal influence on $^{230}Th_{XS}$ deposition

higher Fe_{HT}

lower Fe_{HT}

$^{230}Th_{XS}$ Flux to Sediments (R_P)

1

Distance from Vent (km)
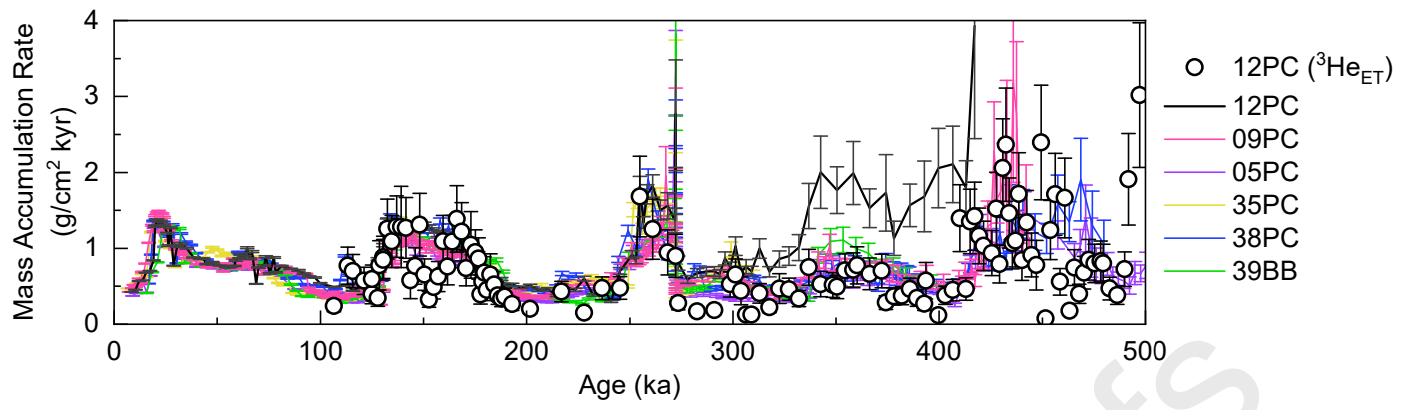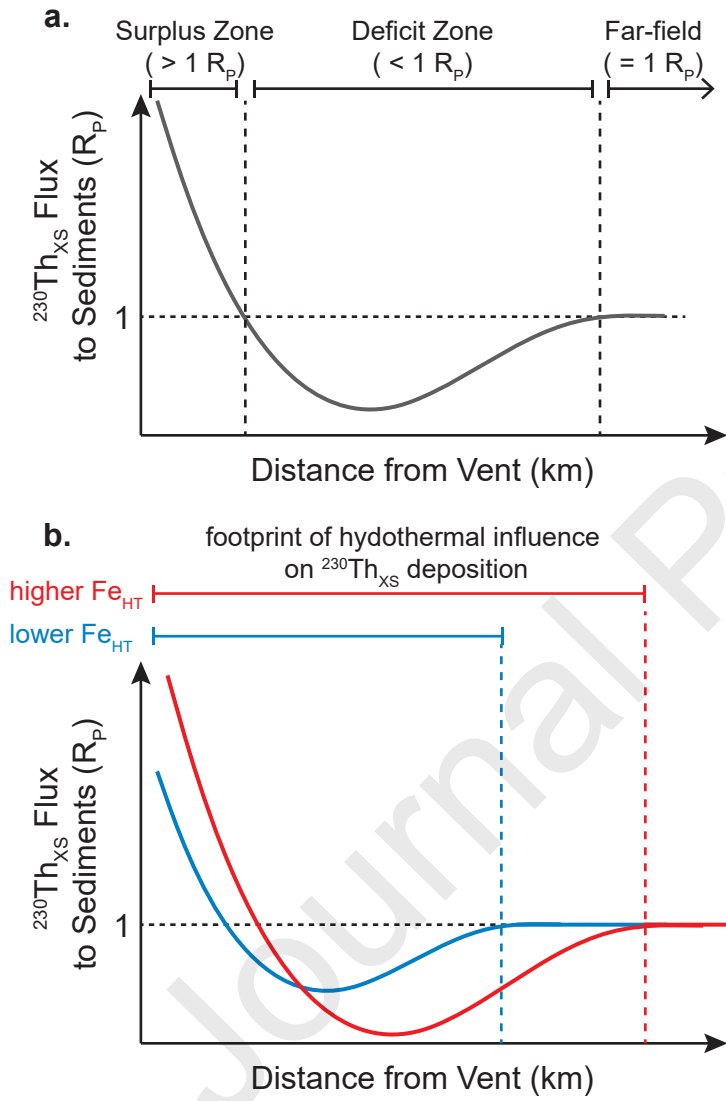
The spatial footprint of hydrothermal scavenging on ^{230}Th$_{XS}$-derived mass accumulation rates

Jennifer L. Middleton[*,] Sujoy Mukhopadhyay, Kassandra M. Costa, Frank J. Pavia, Gisela Winckler, Jerry F. McManus, Marcelle D'Almeida, Charles H. Langmuir, Peter J. Huybers

Highlights
- Near-ridge sedimentary ^{230}Th$_{XS}$ deposition rates constrained using ^{3}He$_{ET}$
- Surplus ^{230}Th$_{XS}$ deposition rates occur in close proximity to vent sites
- Diffusive seawater ^{230}Th transport drives deficit ^{230}Th$_{XS}$ deposition off-axis
- Spatial extent of hydrothermal influence on ^{230}Th$_{XS}$ varies by ridge and over time
- ^{230}Th$_{XS}$ deposition approaches seawater production rate within ~10 km of most ridges

Declaration of interests

☒ The authors declare that they have no known competing financial interests or personal relationships that could have appeared to influence the work reported in this paper.

☐The authors declare the following financial interests/personal relationships which may be considered as potential competing interests: